



**University of
Zurich** ^{UZH}

Vertex Detectors for the Future Circular Collider: Characterising Monolithic Active Pixel Sensors

Author:

Rebekka Wittwer

Supervisors:

Dr. Armin Ilg

Dr. Anna Macchiolo

Prof. Dr. Florencia Canelli

Physics Institute, University of Zurich

Master Thesis in Physics

August 2024

Abstract

The Standard Model (SM) of particle physics is one of the most successful theories of nature, unifying the strong, weak, and electromagnetic forces, however, it still leaves fundamental questions unanswered, many related to the Higgs boson. The Future Circular Collider (FCC), comprising a lepton collider (FCC-ee) and a consecutive hadron collider (FCC-hh), aims to explore these open questions with unprecedented precision. This thesis investigates the feasibility of Monolithic Active Pixel Sensors (MAPS) for the vertex detector of the FCC-ee by characterising the Analogue Pixel Test Structure (APTS), designed for the Inner Tracking System upgrade (ITS3) of the ALICE experiment, which shares similar requirements.

APTS variants were evaluated through lab measurements at the University of Zurich and test beams at CERN's Proton Synchrotron and Super Proton Synchrotron. The measurements focussed on characterising the charge collection properties, spatial resolution, and detection efficiency under various conditions, including different pixel pitches, bias voltages, irradiation levels and pixel geometry.

The results indicated that all APTS versions efficiently collected all generated charge, with the *larger n-well collection electrode* pixel geometry showing greater susceptibility to noise. All variants achieved 99 % detection efficiency and the 10 μm pitch sensors met the spatial resolution requirement of less than 3 μm , crucial for the FCC-ee vertex detectors. Furthermore, APTS was shown to maintain a detection efficiency of over 99 % up to an irradiation of 10^{14} 1 MeV n_{eq} cm^{-2} , reaching the radiation hardness requirements of the FCC-ee.

The findings support the feasibility of MAPS for future high-precision collider experiments, providing a promising foundation for the vertex detector development of the FCC-ee.

Acknowledgments

A huge thank you to the UZH group, particularly Armin and Kunal, for their support, time, and patience throughout this thesis.

A heartfelt thank you to the ALICE ITS3 APTS team, especially Francesca and Giacomo, for their invaluable assistance during the test beam analysis.

A big thank you to my friends and family for their understanding and patience as I excitedly shared details about my work, even when it was beyond their knowledge, and for listening to my complaints after challenging days.

A special thanks to Rebecca for proofreading my entire thesis; any remaining errors are my own, added after she already corrected it.

Lastly (on request of my brother), I extend a special thank you to Schnüru, our cat, for the emotional support, although support and distraction often coincided.

This project has received funding from the European Unions Horizon Europe research and innovation programme under grant agreement No 101057511.

Contents

Abstract	i
Acknowledgments	ii
Introduction	1
1 The Future Circular Collider Project	4
1.1 Accelerating Particles	4
1.2 Future Circular Collider	7
1.3 Experiments at the FCC-ee	10
2 Tracking and Vertex Detectors	14
2.1 Particle Interaction with Matter	14
2.1.1 Energy Loss through Ionisation	15
2.1.2 Multiple Scattering	16
2.2 Tracking and Vertexing	17
2.2.1 Semiconductor Sensors for Tracking and Vertexing	17
2.2.2 Tracking and Vertexing Performance Metrics	19
2.3 Monolithic Active Pixel Sensors	22
2.3.1 ALICE Inner Tracking System 3	22
2.3.2 Vertex Detectors for the FCC-ee	24
2.4 Analogue Pixel Test Structures	26
2.4.1 Measurement Programme	29

3	Characterisation with Radioactive Source	31
3.1	Methods	32
3.1.1	Measurement Setup	33
3.2	Results and Discussion	34
3.2.1	Test-Pulsing	34
3.2.2	^{55}Fe Source Measurements	36
4	Characterisation with Test Beam	40
4.1	Methods	40
4.1.1	Test Beam Setup	41
4.1.2	Analysis with Corryvreckan	42
4.1.3	Temperature Dependence of Alignment	47
4.2	Results and Discussion	48
4.2.1	Global Detection Efficiency and Spatial Resolution	49
4.2.2	In-Pixel Detection Efficiency	54
5	Conclusion and Outlook	57
A	Appendix	60
A.1	Spatial Resolution and Global Efficiency	60
A.2	In-Pixel Detection Efficiency	63
	Bibliography	63

Introduction

The Standard Model (SM) of particle physics is one of the most successful theories in science. It unites three of the four fundamental forces of nature, the strong, weak, and electromagnetic force, excluding gravity. It includes all elementary particles, separated into two main categories. The fermions make up all matter, containing the quarks interacting via all three forces and the leptons interacting only via the electromagnetic and weak interaction. The second category consists of the bosons associated with each fundamental force. The gauge bosons serve as mediators for the fundamental interactions between fermions, while the Higgs boson gives mass to elementary particles via its interactions with them.

The model successfully explains a wide range of phenomena: The strong interaction for example holds the quarks and gluons together inside the proton and neutron, and ties them together to form the atomic nuclei. The electromagnetic interaction, on the other hand, holds the electron in an orbit around the nucleus, allowing the formation of atoms — the fundamental building blocks of nature. The weak interaction is responsible for processes like the beta decay and nuclear fusion in stars.

The SM predicted several new particles that were later found experimentally. The latest being the Higgs boson, which was predicted in the 1960s and discovered in 2012 at the Large Hadron Collider (LHC). Adding to the success of the SM and completing it.

Despite its remarkable success, it still leaves fundamental questions unanswered. For example, the SM cannot explain the amount of matter/anti-matter asymmetry observed in nature, why there exist three generations of the fermions or what dark matter is. Most questions left open by the SM are related to the Higgs boson. Studying it with great precision is therefore a high priority of contemporary particle physics.

The current particle colliders, such as LHC, are not optimised for the precision study of the Higgs boson. Not enough Higgs bosons are produced to reach the statistical significance of rare interactions in a reasonable amount of time, and disentangling all the particles produced in the hadron-hadron collisions of the LHC is challenging. A new particle collider is needed, optimised for the study of the Higgs boson, opening doors to discover physics beyond the SM. The Future Circular Collider (FCC) is one of the proposed future collider projects. It is an integrated project consisting of a lepton collider (FCC-ee) and a consecutive hadron collider (FCC-hh), the focus of this thesis is the FCC-ee. Beyond the precision study of the Higgs boson, the FCC-ee aims to also study many electroweak and QCD processes. This makes it a very versatile project that allows for the full study of the SM with unprecedented precision.

Having a new particle collider also means having new experiments which must be able to work in the environment created by the collider and provide results with the necessary precision. A crucial part of these experiments are the tracking and vertex detectors. They track the particle's trajectory, allowing to infer the particle's momentum and charge. Furthermore, vertex detectors are used to reconstruct the position of the interaction point where the particle was created and the secondary vertices of the particle is short-lived and decays within the detector volume. This is essential for the FCC to reach all its physics goals. Therefore, vertex detectors are the focus of this thesis.

Three different detector designs are being studied for the FCC, all of which foresee using Monolithic Active Pixel Sensors (MAPS) for their vertex detectors. ALICE (A Large Ion Collider Experiment) also uses MAPS to upgrade its inner tracking system (ITS3) and has similar requirements as the FCC-ee vertex detector. Joining the ITS3 MAPS development is a great opportunity to test the feasibility of MAPS for the FCC-ee.

The ITS3 project uses MAPS produced in a 65 nm CMOS process. Within the project, the Analogue Pixel Test Structure (APTS) was designed to study a wide range of parameters, like different semiconductor process designs, pixel pitch and radiation hardness. The goal of this thesis is the characterisation of APTS, and therefore studying the feasibility of 65 nm MAPS for the FCC vertex detector.

Chapter 1 introduces the FCC and its detector designs in more detail. After this, Chapter 2 explains how tracking and vertex detectors work and what parameters influence their performance. MAPS get introduced specifically, as well as APTS.

Next, follow two chapters on characterising APTS. Chapter 3 describes the measurements with a radioactive source carried out in the lab at the University of Zurich (UZH). These measurements allow a first understanding of the sensors by studying their charge-collecting properties. Chapter 4 explains the test beam measurements conducted at the CERN Proton Synchrotron (PS) and Super Proton Synchrotron (SPS) facilities, used to determine the spatial resolution and the global and in-pixel detection efficiency of APTS.

Chapter 5 then gives an overall summary, conclusion, and outlook.

1 The Future Circular Collider Project

Several projects have been proposed to succeed the High-Luminosity LHC (HL-LHC) to conduct extensive high-precision studies of the Higgs boson, investigating the open questions of the SM. Among the most promising projects are the *Future Circular Collider* (FCC) [1], the *International Linear Collider* (ILC) [2], the *Compact Linear Collider* (CLIC) [3], the *International Muon Collider* (IMC) [4], and the *Circular Electron–Positron Collider* (CEPC) [5]. All of them have the main goal of studying the Higgs boson in great detail and with ultra-high precision. They are all lepton colliders using different approaches and technologies to accelerate the particles and therefore offer different options to study the SM. The FCC is an integrated project of two subsequent colliders, enabling ultra-high precision studies not only of the Higgs boson but also many other interesting phenomena like flavour physics, QCD and electroweak processes. It is therefore an incredibly versatile project to explore and challenge the current understanding of particle physics by studying all SM particles. The focus of this thesis is the FCC.

The following sections describe how particle accelerators, like the FCC, work, followed by an in-depth description of FCC.

1.1 Accelerating Particles

There are two main options to study the particles of the SM, either through naturally occurring cosmic rays or through collisions generated with particle accelerators. Although cosmic rays can have energies far beyond what current technologies can produce in accelerators, studying them

has a major drawback: A lack of control over which processes occur and at what rate. The processes currently of high interest in particle physics often only occur at very low rates in cosmic rays, making it challenging to precisely study or observe interesting, rare phenomena. Conversely, particle accelerators produce specific particles at high rates, making particle accelerators currently the only option for studying the Higgs boson.

The rate at which a specific process occurs in an accelerator is determined by the luminosity and the process cross-section. The instantaneous luminosity \mathcal{L} is the ratio of the produced rate R of a given process per unit time dt to the cross-section σ , the likelihood the process occurs in nature,

$$\mathcal{L} = \frac{dR}{dt} \frac{1}{\sigma} . \quad (1.1.1)$$

Integrating the instantaneous luminosity \mathcal{L} over time gives the integrated luminosity L .

$$L = \int \mathcal{L} dt = N \frac{1}{\sigma}, \quad (1.1.2)$$

where N is the number of generated interactions for the given process. An accelerator with a higher luminosity produces more collisions per unit time. To reach high precision and to increase the likelihood of discovering rare new processes, a high luminosity collider is preferred.

Collisions can either be produced by directing a beam of accelerated particles onto a fixed, stationary target (fixed target experiments) or by colliding two beams of accelerated particles (collider experiments). The energy at which the particles collide is a crucial parameter, as it determines the processes that can occur and the particles that can be produced as an outcome of these collisions. The centre-of-mass energy, \sqrt{s} , refers to the total energy available for particle interactions in the frame of reference. In collider experiments \sqrt{s} is given by the relativistic energy-momentum relation

$$\sqrt{s} = E_1 + E_2, \quad (1.1.3)$$

where E is the energy of the respective particles in natural units ($c = \hbar = 1$).

If a high \sqrt{s} is required, collider experiments are preferred over fixed target experiments, since they allow accelerating both interacting particles, as opposed to just one particle being hit onto a fixed, stationary target, where \sqrt{s} is given by $\sqrt{s} = \sqrt{2E_{beam}m_{target}}$.

To accelerate the particles, there are two main options: linear and circular accelerators. In linear accelerators, the particles pass through a series of radio frequency (RF) cavities, at which they are accelerated by an electric field. Conversely, in circular accelerators, particles traverse through

one or a few RF cavities multiple times. A magnetic field keeps them on a circular trajectory by exerting a Lorentz force on them. If the magnetic field gets adjusted such that the Lorentz force matches the centrifugal force of the particles, they stay on a circular path with a constant radius:

$$\vec{F}_{\text{Lorentz}} = \vec{F}_{\text{centrifugal}}, \quad (1.1.4)$$

$$q(\vec{v} \times \vec{B}) = \frac{mv^2}{r}, \quad (1.1.5)$$

When charged particle trajectories are bent in a magnetic field, however, they undergo bremsstrahlung - the emission of photons. This leads to a reduction of \sqrt{s} in circular colliders. The energy loss due to bremsstrahlung is proportional to the energy E and inversely proportional to the mass to the power of four:

$$\frac{dE}{dx} \propto \frac{E}{m^4}. \quad (1.1.6)$$

Consequently, this primarily affects low-mass particles, such as electrons, at high energies. To combat this, one can either use heavier particles to accelerate or increase the radius of the accelerator. One of the advantages of circular accelerators over linear ones, however, is that by circulating the beam, the particles that did not collide can be recycled for further collisions, rather than being dumped after one collision like in linear accelerators. Additionally, having a circular collider enables to host multiple interaction points (IPs), where the beams are brought into collision, offering the opportunity to have several experiments at the same collider, which can complement and verify each other.

The last significant difference between accelerators is in the particles they accelerate. Lepton colliders generate interactions between elementary particles, meaning that the initial state of the interactions is precisely known, making the reconstruction significantly easier. They provide a clean environment and allow precision studies, for example, of the properties of the Higgs. Moreover, the sum of the momenta of the particles produced is always equal to the \sqrt{s} of the collisions, allowing for the full reconstruction of the collision kinematics. Since linear colliders are barely affected by bremsstrahlung, they usually accelerate leptons, profiting from the clean environment. Circular colliders can be used to accelerate leptons as well, but since they are affected by bremsstrahlung, a good additional option for them is to use heavier particles like hadrons.

Hadron colliders bring composite hadrons into collision, where the actual interaction occurs between the fundamental constituents of the hadrons, the valence and sea quarks and gluons. As a result, the initial state is not well defined and many soft interactions occur, leading to a significant background

of uninteresting events called *pile-up*. This complicates the task of distinguishing interesting, high-energetic collisions from background events, but the possibility of reaching higher center of mass energies makes them a great addition to lepton colliders, since the total cross section at hadron colliders is much larger than of lepton colliders. Circular colliders are very useful because they can be built to accelerate leptons and hadrons consecutively, making them very versatile machines [6].

1.2 Future Circular Collider

The FCC is an integrated project consisting of a circular electron-positron collider (FCC-ee) and a circular hadron collider (FCC-hh) consecutively using the same tunnel. It has a circumference of 91.2 km and is planned to be located in the Geneva basin, for reference see Fig. 1.1.

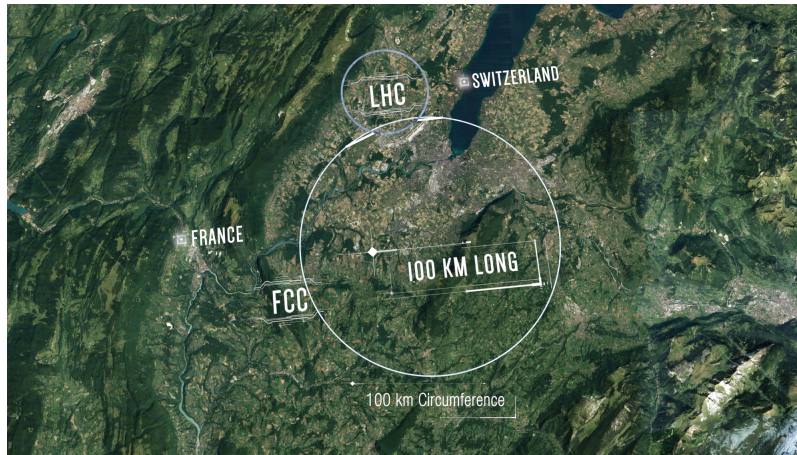


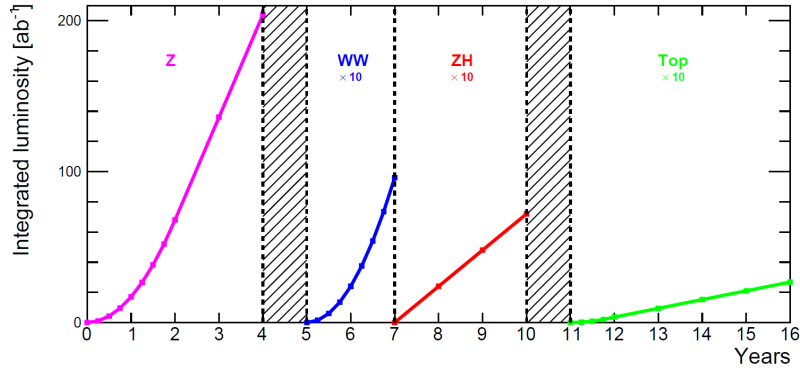
Figure 1.1: Schematic view of the FCC [7].

If approved in late 2027/early 2028, the project would become the successor of the HL-LHC, which is foreseen to end its operation at the end of 2041. The FCC-ee could start data taking in 2045 and the FCC-hh in 2070. Therefore, current research focuses on the feasibility and research and development of detectors for the FCC-ee. Hence, this thesis focusses on the FCC-ee.

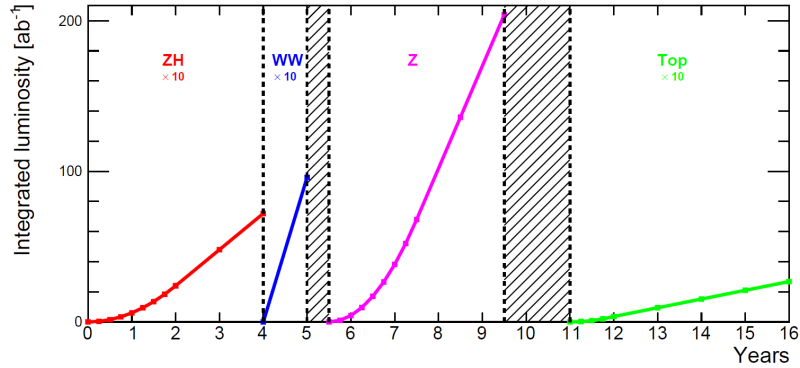
Like the LHC and the Large Electron-Positron Collider (LEP), it has four IPs where the beams of particles get brought into collision, each of which can host one experiment.

The FCC-ee is designed to operate at multiple \sqrt{s} , creating a machine that extends much beyond the sole study of the Higgs boson. The FCC-ee is foreseen to run at a \sqrt{s} of 91, 160, 240 and

350–365 GeV, corresponding to the Z threshold, WW threshold, maximum of ZH production and around the $t\bar{t}$ production threshold. Fig. 1.2 illustrates the foreseen integrated luminosities at each \sqrt{s} . There are currently two possible operation models proposed, the baseline model in Fig. 1.2a plans the order of operation with increasing \sqrt{s} while the alternative model in Fig. 1.2b starts at the ZH production maximum followed by the WW, Z and $t\bar{t}$ threshold runs. Over a 16-year time frame, both models summed over all four IPs collect 6×10^{12} Z bosons, 2.4×10^8 W pairs, 2×10^6 Higgs bosons and 2×10^6 $t\bar{t}$ pairs.



(a) **Baseline model:** The order of operation increases with \sqrt{s}



(b) **Alternative model:** First run at the ZH production maximum, followed by the WW run, then the Z and $t\bar{t}$ runs.

Figure 1.2: Operation models for the FCC-ee with four interaction points. Integrated luminosity at the Z threshold in pink, at the WW threshold in blue, at the ZH production maximum in red and at the $t\bar{t}$ threshold in green. The dashed blocks indicate the shutdown time needed to prepare the collider for the subsequent run at the next \sqrt{s} [1].

Offering high luminosities for some of the most interesting particles of the SM and providing a clean environment with essentially no pile-up, well-defined initial states and a precisely controllable \sqrt{s} , the FCC-ee allows testing the SM with unparalleled, ultra-high precision. Moreover, the broad range of \sqrt{s} offers a high potential for discoveries with a diverse and extensive physics programme as a Higgs, Electroweak, flavour, and top factory.

Since most of the open questions of the SM are related to the Higgs boson, running at the ZH production maximum and producing a sample of 2×10^6 Higgs bosons is of particular interest. This dataset will significantly enhance the ability to measure various properties of the Higgs boson. For instance, when used alongside FCC-hh, it allows for an accurate determination of the Higgs self-coupling. This detailed, high-precision measurement programme allows model-independent determinations of its couplings, either further supporting the SM or revealing tiny violations from it, hinting towards physics beyond the SM.

Running at the Z threshold not only enables the precise study of many electroweak parameters but also allows extensive flavour physics since the Z boson decays to u, d, s, c and b quark pairs 69.2 % of the time. This, for example, allows the study of rare flavour-changing neutral current (FCNC) processes which are highly suppressed in the SM and are sensitive to physics beyond the SM.

Moreover, the runs at the WW and $t\bar{t}$ thresholds enable the precise measurements of the W boson and top-quark masses, contributing to constraining the electroweak fit, again allowing comparison with the predictions of the SM.

This comprehensive approach not only enhances the precision of existing measurements but, among other things, also enables the study of otherwise unreachable flavour physics, QCD and hadronisation processes, and offers the search for rare or forbidden decays.

Fig. 1.3 compares the luminosity per electricity consumption of different proposed future colliders. The FCC-ee delivers the highest luminosities at the Z, WW and $t\bar{t}$ thresholds, as well as at the ZH production maximum. After the FCC-ee programme, the tunnel of the FCC-ee can be reused to subsequently host the FCC-hh, reaching a \sqrt{s} of 80-120 TeV collecting a total luminosity of 20 ab^{-1} , allowing to probe the SM even further [1, 9].

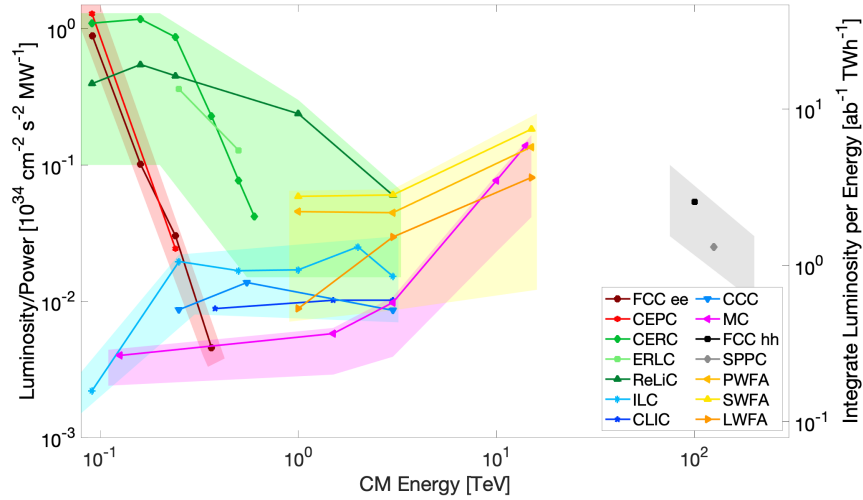


Figure 1.3: Expected luminosity per electricity consumption (over all interaction points) as a function of \sqrt{s} , for future collider projects. The FCC-ee in dark red and the FCC-hh in black [8].

1.3 Experiments at the FCC-ee

The goal in high energy collider experiments is to study particles produced in the collisions. To achieve this, a combination of different detectors is used, each designed to measure a different property of the particles such as momentum, charge, or energy. The combination of all this information enables reconstructing what happened in the collision event and inferring the foundational laws of particle physics. The different detectors are layered around the beam pipe at the IP, measuring the particles as they fly through them.

In the centre of the experiment, positioned nearest to the IP, is a tracking detector. It detects the particle's passage at several points along the particle's trajectory, which enables the reconstruction of the particle *tracks*. At lepton colliders, such as the FCC-ee, the innermost part of the tracking detector is a dedicated vertex detector, to precisely reconstruct the vertices, the points in space where the particles collide (primary vertex) or later decay (secondary and tertiary vertices).

After the tracking detector follow calorimeters, which measure the energy of the particles. They consist of layers of dense materials that initiate showers of secondary particles and layers of sensors in between to measure them. Usually there are two types of calorimeters, an electromagnetic

calorimeter (ECAL) in which particles shower that interact electromagnetically and a hadronic calorimeter (HCAL) where strongly interacting particles produce a shower. The total energy deposited in the detector is proportional to the energy of the incoming particle. Calorimeters perform destructive measurements because to measure a particle's total energy, it has to transfer all of its energy to the calorimeter.

A magnet is either placed before or after the calorimeters. It creates a magnetic field that bends the trajectories of the charged particles. The direction of the curvature indicates the charge of the particle, its momentum can be determined from the curvature of its track, as measured by the tracking detector.

On the very outside are muon detectors. Having muon detectors as the outermost layer of the experiments allows for an easy identification of them, since muons are relatively heavy and live long enough to pass through the other detection layers, while most other particles get stopped in the calorimeters.

The specific traces different kinds of particles leave in the components of the detector allow to separate and identify them, examples of traces that different particles leave can be seen in Fig. 1.4.

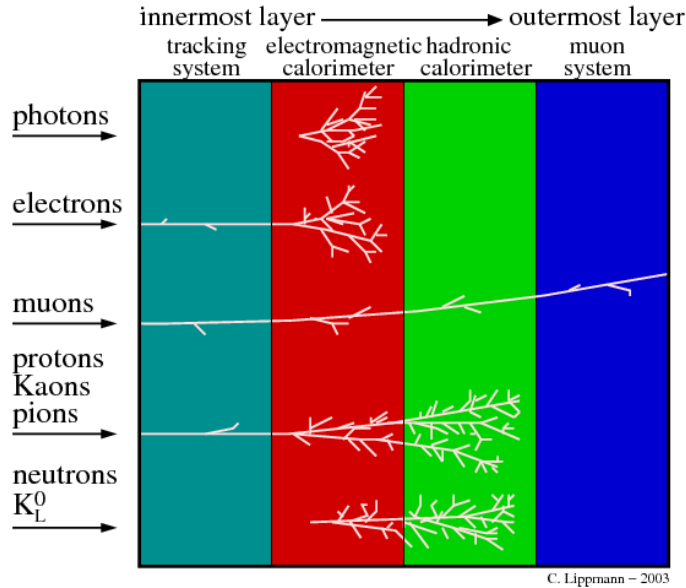


Figure 1.4: Components of a general particle physics experiment. Each particle type leaves a unique signature in the detector components [10].

Currently, three different detector concepts are being studied and optimised for the FCC-ee. They are the *Innovative Detector for Electron-positron Accelerators* (IDEA) [11], an adaptation on a detector designed for CLIC called *CLIC-Like Detector* (CLD) [12] and *A lepton coLLider with highly Granular calorimetry Read-Out* (ALLEGRO) [13] a detector with a noble liquid ECAL. All three designs follow the general set-up described above.

The **IDEA** detector is depicted in Fig. 1.5. Its tracker consists of a silicon pixel vertex detector followed by a large-volume drift chamber surrounded by a layer of silicon microstrip or pixel detectors. The tracker is used for vertexing, tracking, and particle identification using the time-of-flight technique [14]. After the tracker follows an ultralight, thin, and therefore radiation-transparent superconducting solenoid magnet that provides a 2 T magnetic field to bend the particles' trajectory. The calorimeter is positioned after the magnet. It is a dual-readout calorimeter which is sensitive to scintillator and Cherenkov light, providing excellent energy resolution for electromagnetic as well as hadronic showers. The outermost layers are the muon detectors in the magnet's return yoke [1, 11].

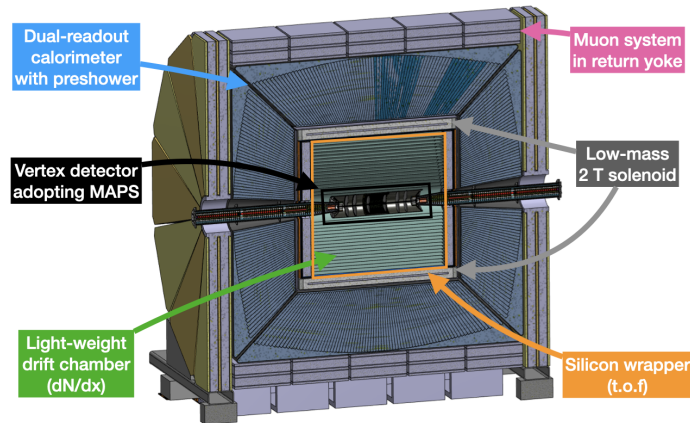


Figure 1.5: Schematic of the IDEA detector [15]

CLD follows a similar setup, it also has a silicon pixel vertex detector and a silicon tracker instead of a drift chamber. It features a highly granular calorimeter and the magnet is positioned after the calorimeter, also providing a 2 T magnetic field. The outermost layers are again muon detectors in the magnet's return yoke [1].

ALLEGRO is the newest proposal. Like IDEA and CLD it uses a silicon pixel vertex detector, the main tracker will either be gaseous or silicone based. The calorimeter is based on a high granularity liquid noble gas ECAL [1, 13].

The focus of this thesis is on the vertex detectors. They are essential to reconstruct the primary and secondary vertices. Accurate vertex detection is particularly essential for lifetime measurements and flavour tagging. Flavour tagging is needed because quarks, due to colour confinement, do not exist alone. When a single quark is produced in a collision, it undergoes hadronisation, generating an ensemble of hadrons that form a jet. Vertex detectors are used to identify the original quark responsible for the jet. Some mesons, such as the B mesons, have a significant lifetime that allows them to travel a measurable distance before decaying, creating a secondary vertex in the detector. The precise determination of the vertex positions is crucial for accurate event reconstruction. Therefore, vertexing is important for processes with hadronic final states, making it especially essential for the measurements of the Higgs couplings to quarks and the flavour physics measurements. All proposed detector concepts foresee the use of Monolithic Active Pixel Sensors (MAPS) for their vertex detectors. Hence, the focus of this thesis is on such MAPS. In the following chapter, vertex detectors are discussed in detail, outlining how they work and what parameters influence their performance.

2 Tracking and Vertex Detectors

Accurate vertex reconstruction is essential for the FCC-ee to reach its physics goals. This chapter first shows how particles interact with matter, explaining how tracking and vertex detectors work and what parameters influence their performance. This motivates the requirements for the FCC-ee and the necessity for the Monolithic Active Pixel Sensor (MAPS) technology, which is introduced next.

The upgrade of ALICE's inner tracking system (ITS3) [16] also uses MAPS and has very similar requirements to the FCC-ee vertex detectors, making the ITS3 MAPS interesting for FCC-ee. Lastly, the Analogue Pixel Test Structure (APTS) is introduced, which is a MAPS with an analogue read-out developed by ALICE ITS3 to characterise the 65 nm CMOS technology. The characterisation of APTS is the objective of this thesis.

2.1 Particle Interaction with Matter

As particles traverse through matter, they undergo interactions that can be measured and utilised to detect them. However, these interactions also perturb the particles, impacting the very thing that is intended to be measured.

Particles interact with matter by depositing energy through electromagnetic or nuclear processes. Charged particles lose energy through scattering, ionisation and excitation of atoms, as well as bremsstrahlung and to a lesser degree through Cherenkov and transition radiation. Photons, on the other hand, interact through the photoelectric effect, Compton scattering, and pair production.

2.1.1 Energy Loss through Ionisation

Tracking and vertex detectors exploit the ionisation of their material to detect traversing particles. A particle with enough energy to ionise matter (minimal ionising particle, MIP) generates electron-hole pairs in the material when traversing it, generating a measurable signal. The ionisation of the material leads to a small energy loss by the particle. The Bethe-Bloch formula describes the mean energy loss due to ionisation per unit length of material the particle travelled through:

$$-\frac{dE}{dx} = 2\pi N_A r_e^2 m_e c^2 \rho \frac{Z}{A} \frac{z^2}{\beta^2} \left(\ln \frac{2m_e \gamma^2 V^2 W_{\max}}{I^2} - 2\beta - \delta - 2\frac{C}{Z} \right). \quad (2.1.1)$$

Here, r_e is the classical radius of the electron, $\gamma = 1/\sqrt{1-\beta^2}$ the Lorentz factor, $\beta = v/c$ the particle's speed relative to the speed of light c , N_A the Avogadro constant and Z and A the atomic and mass number of the material. ρ is the density of the material and z is the charge of the particle in units of the elementary charge e . I is the mean excitation energy of the material (depends on Z) and W_{\max} is the maximum energy transferred in a single collision.

The last two terms are corrections. δ is a correction on the density due to polarisation at high velocities, and C is a shell correction at low velocities due to the breakdown of the assumption that the electron is at rest.

The energy loss around the momentum of a MIP in different materials is plotted in Fig. 2.1 [17]. The energy loss depends on the amount of material through which the particle travels, corresponding to the material budget of the vertex or tracking detector. The energy loss in the tracker should be minimised, as not to interfere with the measurement of the calorimeter. Hence, the material budget of the tracking and vertex detector should be minimised.

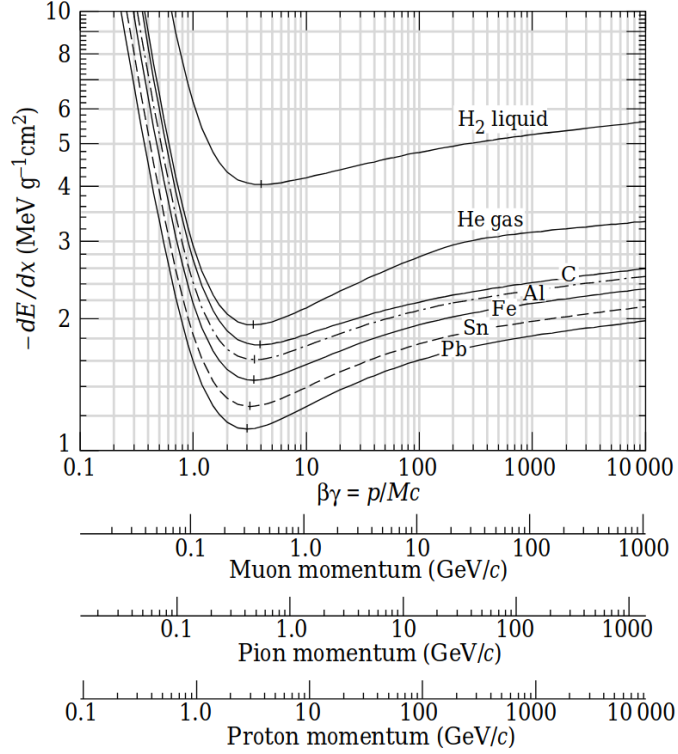


Figure 2.1: Energy loss rate around the momentum of minimal ionising particles in different materials and momenta [17]

2.1.2 Multiple Scattering

In addition to energy loss through ionisation, tracking also gets influenced by multiple scattering. It occurs mostly due to repeated elastic Coulomb scattering from nuclei and some strong interactions for hadrons. Considering that nuclei usually have a mass greater than the incoming particle, the energy transfer is negligible, but each scattering adds a small deviation to the incoming particle's trajectory. Even if this deflection is small, the sum of all the contributions adds a random component to the particle's path. A parallel beam of particles therefore gets an angular spread. The width of the accumulated angular deflection in the xy -plane due to multiple scattering is given by:

$$\theta_{\text{RMS}} = \frac{13.6 \text{ MeV}}{\beta pc} z \sqrt{\frac{x}{X_0}} \left(1 + 0.038 \ln \left(\frac{x}{X_0} \right) \right). \quad (2.1.2)$$

Where x is the thickness of the traversed material and X_0 is the radiation length, the mean length of a given material over which an electron loses $1/e$ of its energy. x/X_0 is therefore the material budget contribution of one layer of one material [17].

As for the energy loss through ionisation, the effect of multiple scattering on the tracking quality gets reduced by minimising the material budget of the detector.

2.2 Tracking and Vertexing

Tracking detectors play a crucial role in particle physics experiments. They not only allow the reconstruction of the particle's trajectory and momentum but are also essential to reconstruct primary and secondary vertices, making them crucial for the FCC-ee to reach its physics goals. All future collider vertex detectors and many trackers foresee to use of semiconductor sensors.

2.2.1 Semiconductor Sensors for Tracking and Vertexing

Tracking and vertex detectors measure traversing particles through the ionisation of their material. When a particle ionises the material, the generated e^- and ions create a measurable signal. One of the most common materials for tracking and vertex detectors is silicon. The sensors tested in this thesis are silicon-based, and therefore the rest of this chapter focusses on this.

However, pure silicon is not suitable for a tracking or vertex detector, since it's neither a good insulator nor conductor. By introducing impurities, the conductivity can be increased and controlled. This method involves adding atoms that have one fewer valence electron compared to silicon, thus creating an extra hole in the lattice structure, referred to as p-type doping. Alternatively, atoms with an extra valence electron are added, which introduces an additional free electron into the lattice, this is known as n-type doping.

Silicon tracking detectors work by doping silicon to turn it into a diode. A diode is formed by a pn-junction where p-type and n-type doped silicon meets. At this junction, holes on the p-type side combine with electrons on the n-type material, creating a region without charge carriers - the depletion region, as illustrated in Fig. 2.2. Within the depletion region, there are localized negative and positive charges, creating an electric field. Applying a voltage in the direction of minimal current flow across the depletion region—known as a reverse bias voltage—increases the thickness of the depletion region.

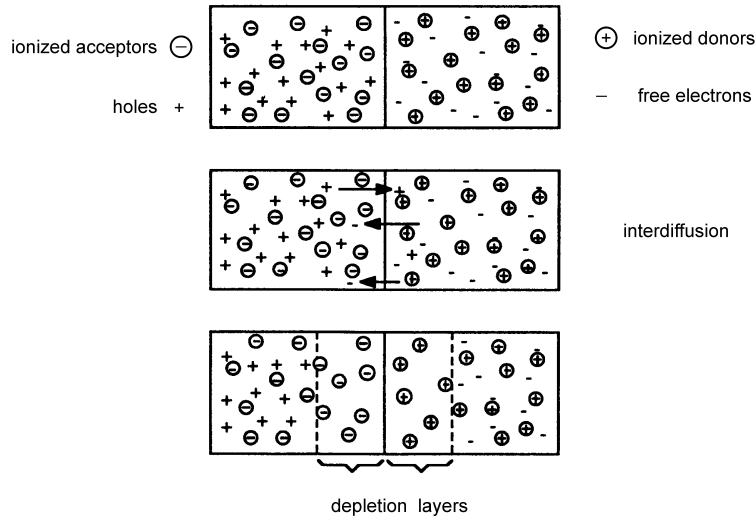


Figure 2.2: At the pn-junction, holes from the p-type region combine with electrons from the n-type region, resulting in a depletion region without free charge carriers. This region is characterised by localised positive charges on the n-type side and localised negative charges on the p-type side [18].

As charged particles pass through the depletion region, they ionise the silicon and create electron-hole pairs, see Fig. 2.3. For partially depleted devices, the electrons generated outside the depletion region are collected primarily by diffusion before being collected by the strong drift field in the depleted zone around the collection electrode. This is a relatively slow process and is susceptible to charge trapping in defects caused by radiation damage, meaning some signal charge can get lost. Charge carriers in fully depleted devices drift to the collection electrodes at the detector’s surface, where the created signal gets amplified, shaped, and measured. Hence, it is preferable to have a depletion region throughout the sensitive layer such that all charge carriers are transported to and measured at the collection electrode and that the collection time and the effects of radiation damage caused by non-ionising radiation are reduced [19].

A pixel is the smallest unit of a detector that can independently register a signal. The distance from the centre of one pixel to the centre of an adjacent pixel is called the pixel pitch. The generated charge can diffuse and may be collected by neighbouring pixels, causing a particle to generate signals across several pixels and form a cluster. The hit position of the traversing particle is then calculated from the charge-weighted centre of the cluster. Charge sharing enhances the spatial

resolution compared to the binary resolution, where a particle generates a signal in only one pixel. The binary resolution of the detector, considering a uniform probability distribution, is given by $\text{pitch}/\sqrt{12}$. This represents the minimal spatial resolution of a silicon tracking detector without any charge sharing.

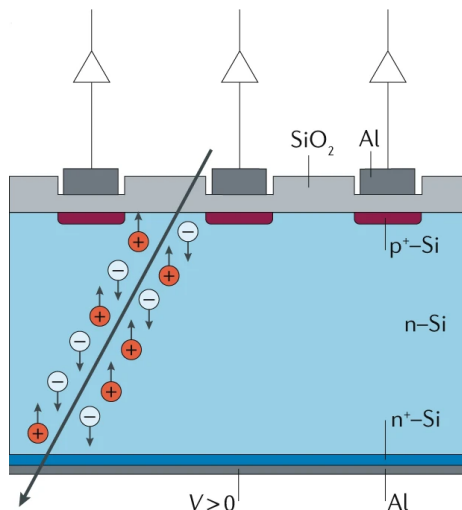


Figure 2.3: Schematic operation of a silicon tracking detector [20].

2.2.2 Tracking and Vertexing Performance Metrics

There are several parameters of tracking and vertex detectors directly influencing the tracking and vertexing performance. The spatial resolution — the accuracy with which a sensor can measure the position of a traversing particle — is one of the most fundamental ones. Another important parameter is the detection efficiency, the likelihood of measuring a traversing particle. A crucial parameter for vertex detectors is the resolution of the impact parameter. The transverse impact parameter, d_0 , is defined as the shortest perpendicular distance from a track to the primary vertex, see Fig 2.4. The precision of the vertex reconstruction strongly depends on the impact parameter resolution, making this a crucial parameter for the FCC-ee vertex detector.

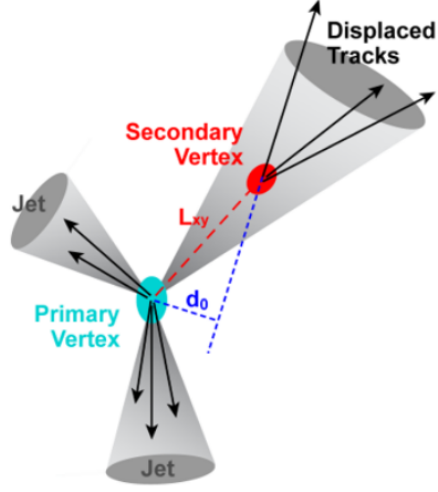


Figure 2.4: Illustration of a collision where three jets emerge from the primary vertex. One jet has a secondary vertex, where a particle decayed after some time. The transverse impact parameter, d_0 , is defined as the shortest distance from a track to the primary vertex [21].

A simple two-layer detector system, as shown in Fig. 2.5, easily demonstrates which parameters of a vertex detector influence the resolution of the impact parameter the most. First, assuming in Fig. 2.5a that the outer layer (layer 2), at distance r_2 , has a perfect spatial resolution, i.e. $\sigma_2 = 0$, the resolution of the impact parameter, σ_{d_0} , is then determined by the resolution of the first layer (layer 1), σ_1 . The aspect ratio of the two layers is:

$$\frac{\sigma_{d_0}}{\sigma_1} = \frac{r_2}{r_2 - r_1}. \quad (2.2.1)$$

Now in Fig. 2.5b, assuming that the first layer, at distance r_1 , has perfect resolution, i.e. $\sigma_1 = 0$, leads to

$$\frac{\sigma_{d_0}}{\sigma_2} = \frac{r_1}{r_2 - r_1}. \quad (2.2.2)$$

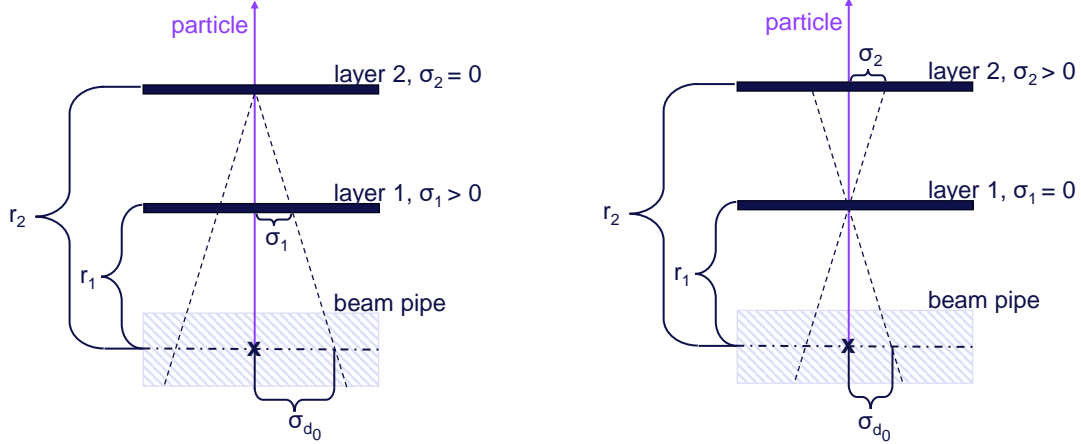
Adding the two contributions to σ_{d_0} in quadrature and including a term for multiple scattering gives

$$\sigma_{d_0}^2 = \left(\frac{r_1}{r_2 - r_1} \sigma_2 \right)^2 + \left(\frac{r_2}{r_2 - r_1} \sigma_1 \right)^2 + \sigma_{\text{MS}}^2. \quad (2.2.3)$$

The impact parameter resolution can be expressed for generally with the following parametrisation:

$$\sigma_{d_0} = a \oplus \frac{b}{p \sin^{3/2} \theta} \quad (2.2.4)$$

where a is related to the single hit resolution of the sensor and $\frac{b}{p \sin^{3/2} \theta}$ represents the contribution of multiple scattering. Here, p is the particle momentum and θ is the polar angle of the particle's trajectory.



(a) configuration assuming layer 2 is an ideal detector ($\sigma_2 = 0$)

(b) configuration assuming layer 1 is an ideal detector ($\sigma_1 = 0$)

Figure 2.5: Idealized two layer detector. \times marks the interaction point. σ_{d_0} is the extrapolated interaction point of the track at the impact parameter, r_1 and r_2 are the distance of the middle of the beam pipe to layer 1 and layer 2 respectively [22].

This shows that the innermost layer of a vertex detector must be as close to the primary vertex as possible (r_1 small), its spatial resolution (σ_1) is crucial, and the material measured in radiation lengths x/X_0 must be as small as possible, see Eq. 2.1.2 [22].

This again indicates how important the reduction of the material budget is to improve the performance of the vertex detector.

In addition, a vertex and tracking detector is an integral component of an overall project that encompasses an accelerator, physics objectives, and a comprehensive detector system as outlined in Section 1.3. This adds many more factors, which impose further constraints on the tracking and vertex detector. Other parameters to consider might be power consumption or radiation tolerance.

2.3 Monolithic Active Pixel Sensors

As described above, the material budget of the vertex detector is an influential parameter on its performance. To reach the FCC-ee needed vertex reconstruction resolution, it is essential to have a minimal material budget of the vertex detector.

Traditional hybrid sensors have the read-out electronic separated from the sensing layer and connect them through bump bonding. MAPS combine the read-out electronics into the same piece of silicon as the sensing layer, presenting several advantages over traditional hybrid pixel detector technologies, as they are cheaper to build, can be thinned down without having the additional material from the read-out electronic, therefore reducing the material budget, and operate with low power consumption. Additionally, they can be made reasonably radiation hard [23].

MAPS can be fabricated in a commercial CMOS process and were shown as a promising technology for high-granularity and light material budget detectors. ALICE is the first experiment at the LHC to use this technology. ALICE's current inner tracking system (ITS2) uses a MAPS named ALPIDE [24], which is produced in the TowerJazz 180 nm CMOS process. The innermost three layers of the tracker use MAPS that are 50 μm thick. These are attached to a flex cable made of aluminium and mounted on a mechanical support and cooling structure (water cooling), which together amounts to a material budget of 0.35 % x/X_0 per layer [24].

The ALPIDE can only be partially depleted, meaning that the charge is mainly collected by diffusion. This affects the charge collection time and makes it susceptible to charge trapping in high-radiation environments. The next generation of MAPS are therefore moving in the direction of fully depleted MAPS. Full depletion means that the charge is collected by drift and hence features better radiation hardness and faster charge collection [25].

ALICE is planning the upgrade of ITS2 during the upcoming Long Shutdown 3 (2026-2029) of the LHC. Extensive studies are being conducted on fully depleted MAPS for the new inner tracking system 3 (ITS3), which will replace the three innermost layers of ITS2.

2.3.1 ALICE Inner Tracking System 3

The main goals of ITS3 are to reduce the material budget from the current 0.35 % x/X_0 to 0.05 % x/X_0 per layer and to place the first layer at a radial distance of only 18 mm from the IP instead of the current 22 mm. This will boost the impact parameter resolution by a factor of

two over all momenta and drastically enhance the tracking efficiency at low transverse momentum, as can be observed in Fig. 2.6.

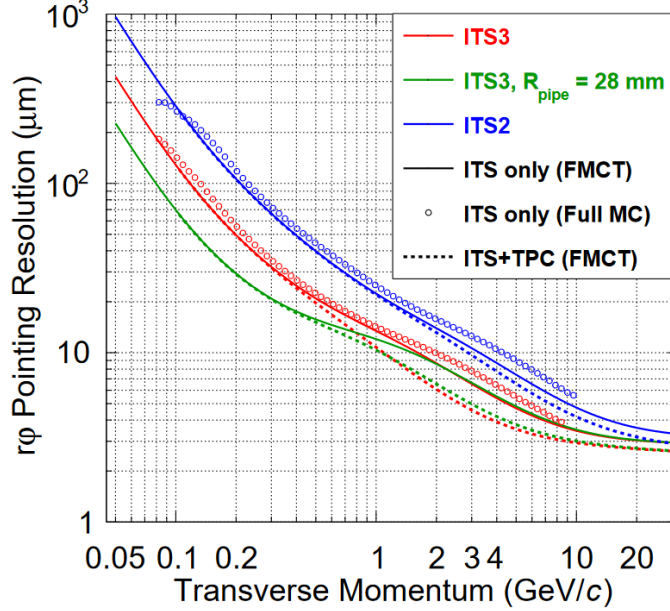


Figure 2.6: $r\phi$ pointing resolution for primary charged pions as a function of the transverse momentum. The current system, ITS2, in blue and the proposed ITS3 upgrade in red. The green curve (ITS3, $R_{\text{pipe}} = 28$ mm) refers to an even further upgrade with a detector configuration where the two innermost layers are placed inside the beam pipe [26].

To achieve these goals, a new sensor is needed that minimises or removes powering and readout cables, cooling elements, and mechanical support structures. The only components remaining, to reach the very minimal material budget, are the silicon sensors and very light-weight carbon-foam support structures. The sensors are deploying the commercial TPSCo 65 nm CMOS ISC imaging technology and a recent technique called stitching. Stitching extends the sensor beyond one single mask used in the photo-lithographic process of chip manufacture, enabling the production of chips reaching dimensions of $27 \text{ cm} \times 9 \text{ cm}$ on 12-inch diameter silicon wafers. The sensors are then thinned down to $50 \text{ }\mu\text{m}$ or below, allowing the silicon to be bent. In this way, cylindrical layers can be built and due to the low power consumption of the MAPS further improved by moving to the

65 nm CMOS process, only air flow cooling is needed, again minimising the material budget. An installation model of ITS3 can be seen in Fig. 2.7 [27].



Figure 2.7: Installation model of all three layers of ALICE ITS3 [15]

The requirement on the MAPS used for ITS3 are a spatial resolution better than $5 \mu\text{m}$, particle detection efficiency larger than 99 % after an exposure to around $10^{13} \text{ 1 MeV n}_{\text{eq}} \text{ cm}^{-2}$ of Non Ionising Energy Loss (NIEL) [16].

2.3.2 Vertex Detectors for the FCC-ee

The requirements for ITS3 are very similar to the vertex detector requirements for the FCC-ee. The FCC-ee, as a high luminosity circular collider aimed at studying a broad spectrum of processes with ultra-high precision, imposes strict demands on the vertex detectors. The clean environment in which the Higgs boson will be produced gives a unique opportunity to explore all decay modes, hence the importance of excellent b and c tagging and τ reconstruction, for which vertex reconstruction is essential. Beyond the precision study of the Higgs boson, flavour physics also requires excellent vertex reconstruction. This makes the performance of the vertex detectors critical for the FCC-ee to reach its extensive and diverse physics goals [25].

The ITS3 vertex detector requirements are very similar to the ones of the FCC-ee, as can be seen in Tab. 2.1. For example, the FCC-ee aims at a slightly better spatial resolution, while the material budget and power density can be somewhat larger, the radiation tolerance of NIEL is the same. ITS3, therefore, offers the opportunity to test the feasibility of the FCC-ee vertex

2.3. MONOLITHIC ACTIVE PIXEL SENSORS

Requirements	ALICE ITS3	FCC-ee
Spatial resolution	5 μm	3 μm
Material budget x/X_0 per layer	0.07 %	0.3 %
Radiation tolerance NIEL	10^{13}	10^{13}
First layer radius	19 mm	13.7 mm
Power density	40 mW/cm ²	100 mW/cm ²

Table 2.1: Vertex detector requirements comparison between ALICE ITS3 and FCC-ee [1, 16]

detector requirements, as well as exploring the possibility to go beyond the current requirements, which could improve the FCC-ee performance significantly. How a further reduction of the material budget would impact the impact parameter resolution can be seen in simulation shown in Fig. 2.8. This thesis therefore characterises sensors developed for ALICE ITS3, but its focus is on their feasibility for the FCC-ee.

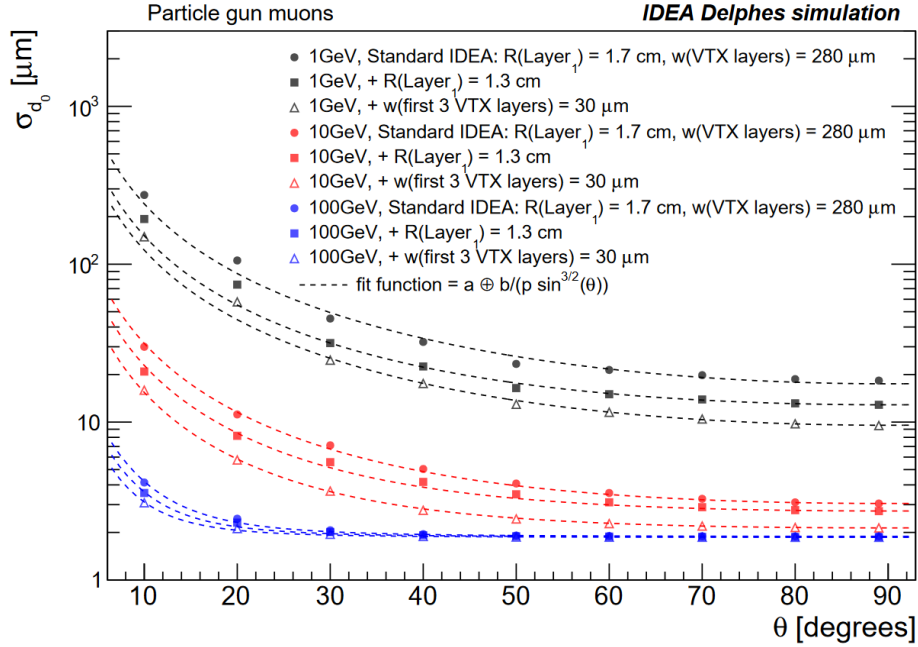


Figure 2.8: Effect of reduced material budget on the impact parameter resolution, d_0 , in the FCC-ee done in Delphes fast simulation [15, 28]

2.4 Analogue Pixel Test Structures

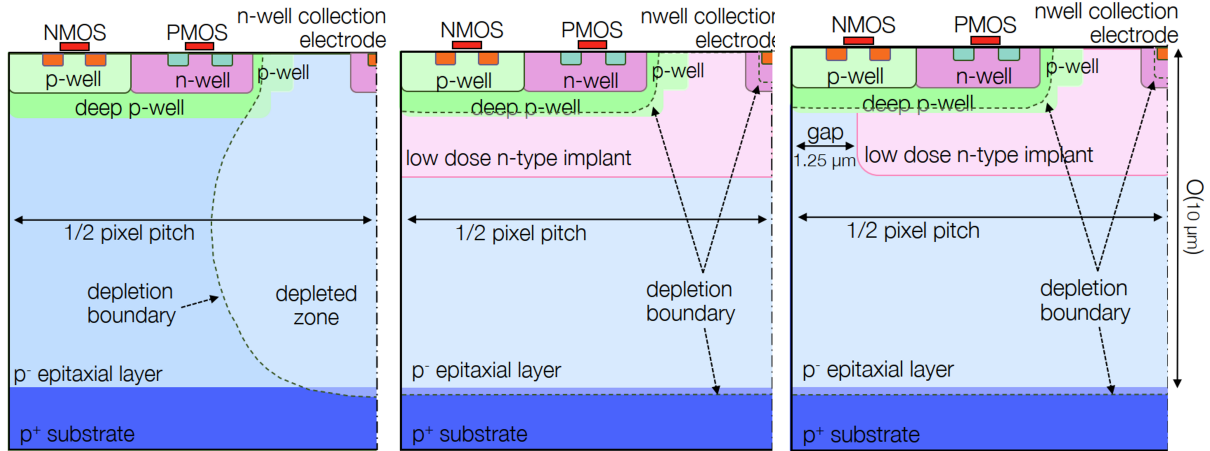
For the current vertexing sensors of ALICE, the ALPIDE, three process designs—standard, modified, and modified-with-gap—were explored to investigate charge collection properties of the Tower-Jazz 180 nm CMOS process. The same three processes are investigated now for the TPSCo 65 nm CMOS ISC process of ITS3 [29].

The **standard** process features a deep p-well that ensures that only the small n-well collection electrode is unshielded from the epitaxial layer, allowing it to collect signal charge, while the other PMOS and NMOS transistors, containing the circuitry, are prevented from collecting charge, see Fig. 2.9a. This enables the full use of the CMOS circuitry. The low capacitance of the small collection electrode reduces power consumption. However, the depletion region is only balloon-shaped around the collection electrode. Although signal charge generated outside the depletion region is still collected by diffusion, a drift field, and hence depletion over the full sensitive layer is needed for fast charge collection and better radiation hardness [30].

The **modified** process, illustrated in Fig. 2.9b, reaches full depletion by adding a deep low-dose n-type implant under the entire area of the pixels. The depletion region then starts from the newly created junction and extends across the entire area of the pixels. Increasing the reverse bias voltage will then further extend the depletion towards the collection electrode. However, the electric field still reaches a minimum in the corners of the pixels, resulting in a degraded timing resolution and efficiency loss after irradiation [30].

The **modified-with-gap** process, shown in Fig. 2.9c, introduces a gap in the deep n-type implant at the pixel boundaries. This increases the lateral electric field and shifts the minimum of the electric field deeper into the silicon by introducing another junction. Therefore, the charge sharing among pixels is reduced and the drift path is shortened, leading to faster charge collection [31].

2.4. ANALOGUE PIXEL TEST STRUCTURES



(a) **Standard process:** A deep p-well shields the CMOS circuitry from collecting charge, and the low capacitance of the small collection electrode results in lower power consumption. The depletion region is balloon shaped.

(b) **Modified process:** The additional low dose n-type implant leads to full depletion of the device.

(c) **Modified-with-gap process:** Gaps are introduced in the low dose n-type implant at the pixel boundaries, giving more control over charge sharing between pixels.

Figure 2.9: The cross-section of one half of a pixel of each process [29]

The transition from the TowerJazz 180 nm CMOS process of the ALPIDE to the TPSCo 65 nm CMOS ISC process for ITS3 requires the optimisation of sensor yield, charge collection and radiation hardness in the new process. To study this, three prototype chips were produced: the *Analogue Pixel Test Structure* (APTS) [19], the *Circuit Exploratoire 65* (CE65) [32], and the *Digital Pixel Test Structure* (DPTS) [33]. This thesis focusses on characterising the APTS.

The APTS incorporates a 6×6 pixel matrix with direct analogue readout on the central 4×4 pixels, providing full and fast access to the analogue signal. For the subsequent measurements, only the signal of the four innermost pixels, the seed signal, is considered to avoid edge effects. A photo of an APTS under a microscope can be seen in Fig. 2.10.

The goal of the APTS is to explore the different sensor designs and processes. Consequently, they are available in the three process types described above and each process comes in various versions

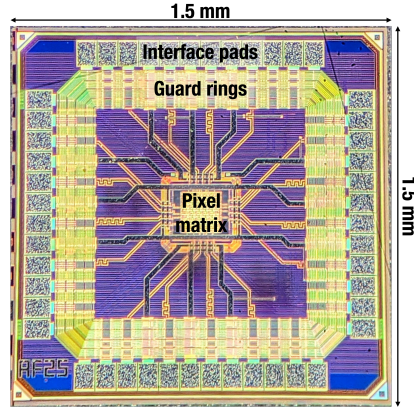


Figure 2.10: An APTS sensor under a microscope [19]

of pixel pitch and irradiation level. They feature four pixel pitches (10, 15, 20, and 25 μm) and allow the application of a reverse substrate voltage, V_{sub} , from 0 to -5 V. Additionally, the *modified-with-gap* process comes in different variants of the geometry and size of the p-well and n-well collection electrode, produced to study the influence on the capacitance, charge collection, and radiation hardness. The variants are a *reference* version, one with a *smaller p-well enclosure*, one with a *finger-shaped p-well enclosure*, and one with a *larger n-well collection electrode*. For comparison, refer to Fig. 2.11 [19].

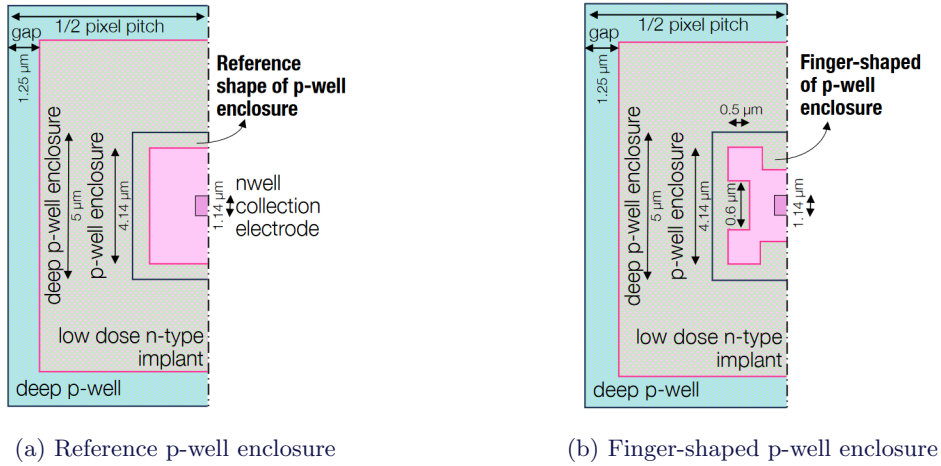


Figure 2.11: Top view of half a pixel for different shapes of the deep p-well [19]

2.4.1 Measurement Programme

The ALICE ITS3 collaboration has already conducted extensive studies on the APTS, examining factors such as pixel pitch, substrate voltage, process design performance, and radiation hardness. The contribution of this thesis is the study of the variants of p-well and n-well collection electrode geometry.

The previous studies on APTS were conducted using chips that contain only the reference matrix, as seen in Fig. 2.10; these are referred to as *p-type* chips. In contrast, the four variants of p-well and n-well collection electrode geometry were implemented on the same chip, on a so-called *multiplexer* chip, as shown in Fig. 2.12. One multiplexer chip contains four different pixel matrices, one of each variant, and powers them simultaneously, although only one matrix can be read out at a time. Having multiplexer chips makes it easier and faster to test the different variants since the chip doesn't need to be swapped out to test a new variant.

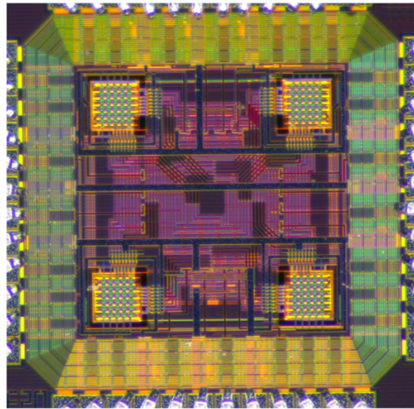


Figure 2.12: An APTS multiplexer sensor under a microscope

The sensor types tested at UZH are listed in Tab. 2.2. All of them have been produced in the *modified-with-gap* process and apart from one all were multiplexer chips. They have pixel pitches of 10 or 20 μm , and the 20 μm chips come in three different levels of irradiation by irradiation with non-ionising radiation (NIEL).

2.4. ANALOGUE PIXEL TEST STRUCTURES

Pitch [μm]	Process Design	Geometry Variant	NIEL [$1 \text{ MeV } n_{\text{eq}}/\text{cm}^2$]
10	modified with gap	reference	None
		larger n-well	None
		finger p-well	None
		smaller p-well	None
20	modified with gap	reference	None, 10^{14} , 10^{15}
		larger n-well	None, 10^{14} , 10^{15}
		finger p-well	None, 10^{14} , 10^{15}
		smaller p-well	None, 10^{14} , 10^{15}

Table 2.2: Characteristics of APTS prototype chips tested at UZH

The goal of this thesis is to study the properties of the sensors and compare the four variants. For this lab measurements with a radioactive source and test beam measurements were conducted. This allows the study of the charge collection properties as well as determining the spatial resolution and detection efficiency of the sensors. The lab measurements with a radioactive source are presented in Chapter 3 and the test beam measurements are detailed in Chapter 4.

3 Characterisation with Radioactive Source

The measurement of the spectrum of a radioactive source gives valuable insight into the charge collection properties and therefore into the depletion of a sensor. When a MIP passes through matter, it loses energy through ionisation, as described in Section 2.1.1, and tracking and vertex detectors exploit this to detect the passage of particles, as elaborated in Section 2.2.1. In a fully depleted device, all the charge generated by the ionisation of the material is collected, whereas in partially depleted devices, some charge may be lost since it recombines in the undepleted volume. By comparing the characteristic spectrum of a source to its measured spectrum, it can be determined whether all charge generated within the detector is collected. Additionally, this enables the determination of a calibration factor by using the measured analogue-to-digital converter (ADC) counts to map the peak positions back to the known emission energies of the source. This enables converting ADC units to the number of electrons (e^-), essential for comparing sensors, by converting the thresholds of the amplitude initially set in ADC units to the number of e^- . Such conversions are necessary for the test beam measurements described in Chapter 4.

The chip itself can induce a charge of approximately 1800 electrons [19] (called a *test-pulse*), therefore, before starting with the measurements of the source spectrum, test-pulsing of each chip was performed, serving as an initial quality assessment to verify the functionality of all pixels and giving a first idea about the charge collection properties. For the subsequent source spectrum measurements, a ^{55}Fe source was used. The measurement methods and setup will be introduced first, followed by the presentation and discussion of the results.

3.1 Methods

^{55}Fe atoms decay through electron capture to Mn-55, with a half-life of 2.737 years, emitting X-rays. The most probable transitions are the Mn- K_α and Mn- K_β peaks, with probabilities of 16.2 % and 8.2 % respectively. An example of a ^{55}Fe spectrum is shown in Fig. 3.1. The very narrow peaks can be treated as a monoenergetic lines. The Mn- K_α peak corresponds to the photon energy $E_\gamma = 5.9$ keV which will be used for the conversion of ADC units to number of e^- .

For the measurement of the ^{55}Fe spectrum only the signal of the four innermost pixels, the seed signal, is considered in order to avoid edge effects. The peaks of the spectrum were fitted with Gaussian functions like in Fig. 3.1, and the mean value of the fitted Gaussian's is then used for the energy calibrations. The amplitude of the pixel signal of each peak is mapped to its corresponding photon energy. This can be fitted with a linear function, with the intercept parameter at 0, as shown in Fig. 3.2.

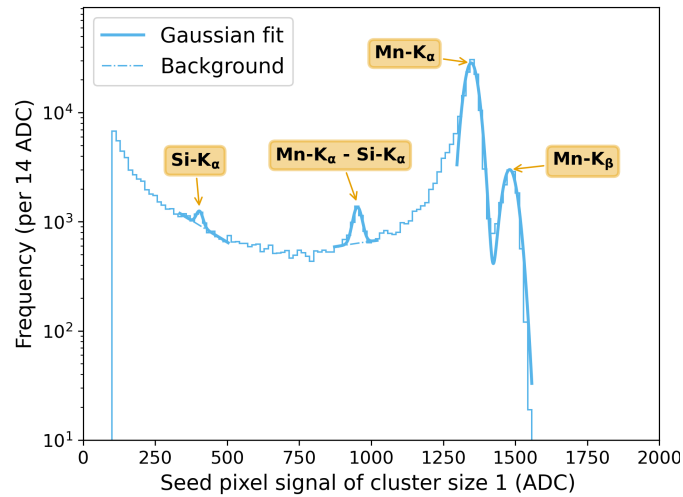


Figure 3.1: Example of the ^{55}Fe spectrum for the seed signal of an APTS, with Gaussian fits of the four peaks: Si- K_α , Mn- K_α - Si- K_α , Mn- K_α and K_β [19].

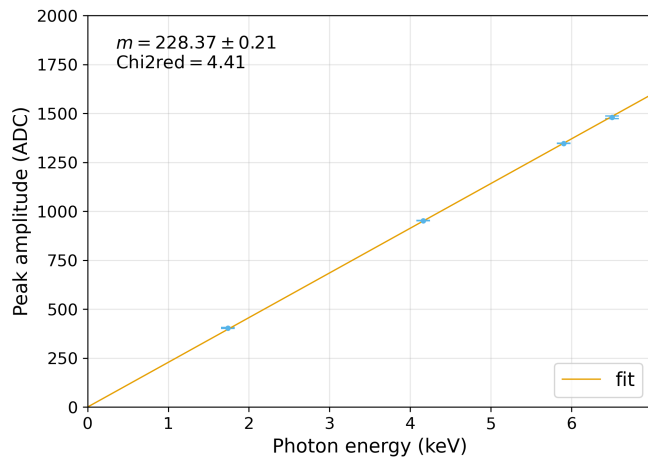


Figure 3.2: Correlation between the seed pixel signal and the photon energy fitted with a linear function for an APTS [19].

3.1.1 Measurement Setup

The measurement setup can be seen in Fig. 3.3. The APTS is on a carrier board which is connected to a custom proximity board and data acquisition (DAQ) board. The DAQ board features a Field-Programmable Gate Array (FPGA) chip to process the incoming data and the proximity board hosts the ADCs and provides power to the sensor. The sensor is cooled with a water chiller, which is set to 14 °C. The goal was not to cool down the sensor, it is supposed to be operated at room temperature, but rather to provide a stable and controlled environment. During the measurements, the sensor is covered to shield it from ambient light.

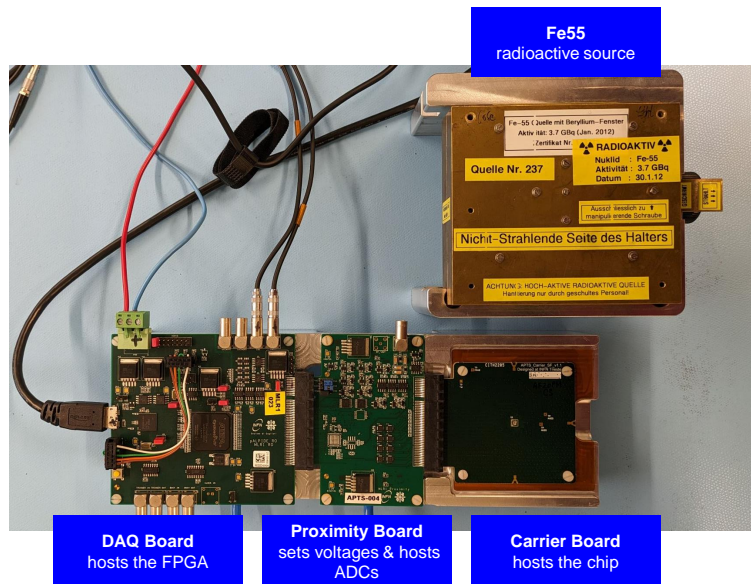


Figure 3.3: ^{55}Fe Source measurement set-up. The carrier board hosts the chip, the proximity board sets the voltages and hosts the ADCs, and the DAQ board is based on an FPGA. During the measurements, the ^{55}Fe source is placed over the carrier board and gets covered to shield it from ambient light.

3.2 Results and Discussion

In this section, the results from the test-pulsing and ^{55}Fe source measurements are presented and discussed. The focus is on the charge collection properties and the impact of different parameters such as pixel pitch, bias voltage, and irradiation levels on the sensors.

3.2.1 Test-Pulsing

In Fig. 3.4, a typical test-pulsing signal can be seen. The amplitude defined as the difference between the baseline (approximately 0 ADC units) and the minimum of the signal (here approximately -1400 ADC units). After reaching the minimum, the signal gradually returns to the baseline. The baseline noise was subtracted, and all baselines were brought to 0 ADC units. All pixels exhibit similar behaviour, having the same signal amplitude and return time.

3.2. RESULTS AND DISCUSSION

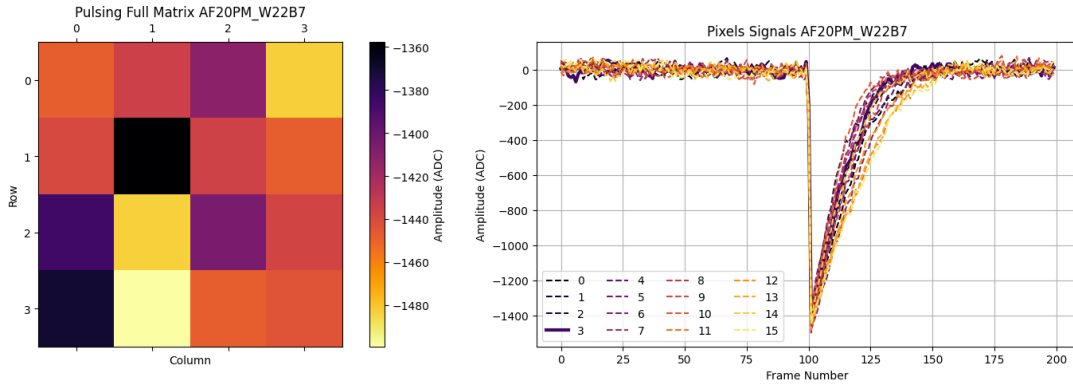


Figure 3.4: **Test-pulsing**: Left: Representation of sensor, each bin is one pixel, the colour illustrates the signal amplitude. Right: Signal measured at each pixel. All pixels behave very similarly, the baseline is around 0 ADC, the amplitude around - 1400 ADC, and they have a similar return time. *Parameters: pitch = 20 μm , $V_{sub} = - 1.2 \text{ V}$, variant = reference, irradiation = none*

Fig. 3.5 shows an example where certain pixels show different behaviour. One pixel doesn't reach the same amplitude as the others, while another takes longer to return to the baseline. These effects could be observed across all variants at different bias voltages but were more prevalent at higher voltages and for irradiated sensors. Such effects were not observed for the p-type sensors and therefore were attributed to the intricacies multiplexer sensors. In multiplexer sensors, four pixel matrices are powered on together, potentially increasing noise causing these effects. However, this seems to be a minor issue, only problematic at higher irradiation levels.

These initial test-pulsing measurements showed that the measurements of the variants might be affected by more noise due to being produced on multiplexer chips. The following ^{55}Fe source measurements will show the impact of the higher noise for irradiated sensors.

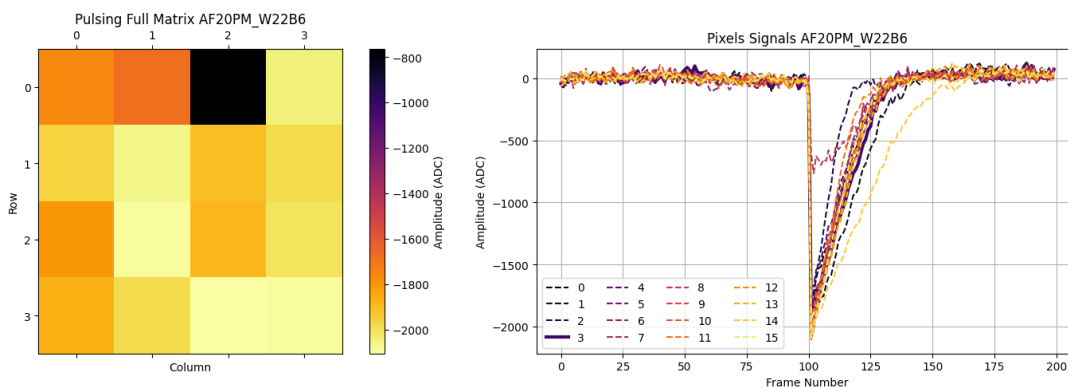


Figure 3.5: **Test-pulsing**: Left: Representation of sensor, each bin is one pixel, the colour illustrates the signal amplitude. Right: Signal measured at each pixel. Some pixels show unusual behaviour, one has a longer return time, another has a lower amplitude. *Parameters: pitch = 20 μm , $V_{\text{sub}} = -4.8 \text{ V}$, variant = reference, irradiation = none*

3.2.2 ^{55}Fe Source Measurements

The ^{55}Fe source measurements provide valuable insights into the charge collection properties and depletion characteristics of the sensors. This section presents and discusses the obtained results, highlighting the effects of pixel pitch, bias voltage, and irradiation levels on sensor performance. For all the following plots, the distributions were normalised by the total number of events and only the seed pixel signal is shown.

Fig 3.6 shows the ^{55}Fe spectrum of the different variants, illustrating how the amplitude is different for the *larger n-well collection electrode* pixel geometry variant due to its higher capacitance. The capacitance affects the signal amplitude in mV, making it appear lower for variants with higher capacitance. By plotting the same data in electrons instead of mV, as illustrated in Fig. 3.7, this effect is eliminated. This is because the conversion to electrons normalises the signal amplitude relative to the capacitance, providing a true representation of the charge collected. Consequently, no visible change in the charge distribution of the different variants can be observed. The subsequent plots will only be shown in electrons to ensure accurate comparisons.

3.2. RESULTS AND DISCUSSION

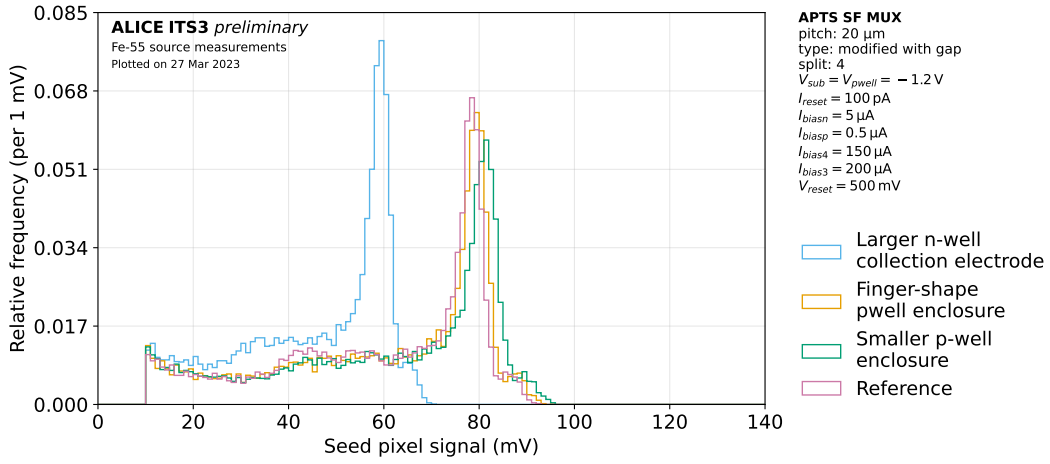


Figure 3.6: **Variant Comparison:** Distribution of seed signal in mV for different sensor variants. The *larger n-well collection electrode* has a lower signal in mV than the other variants due to having a higher capacitance [19].

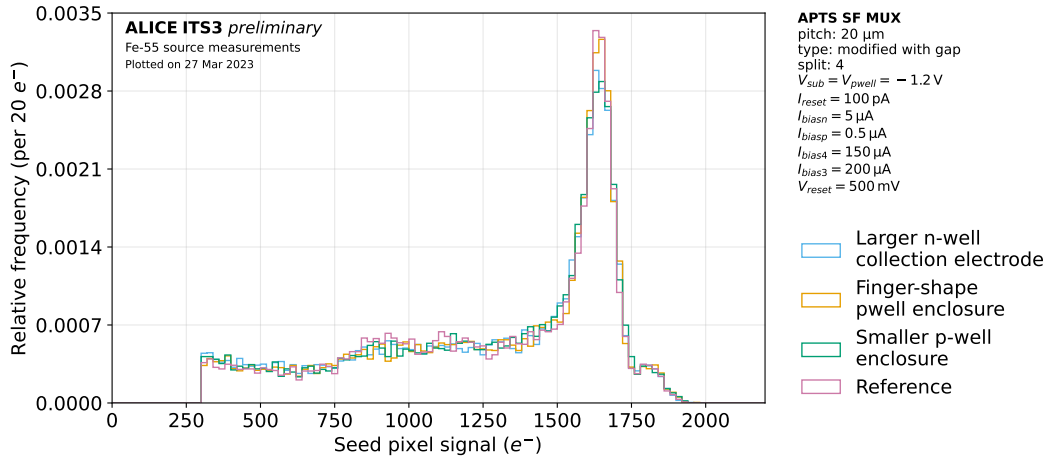


Figure 3.7: **Variant Comparison:** Distribution of seed signal in e^- for different sensor variants. The sensors show similar charge collection properties for all four variants [19].

3.2. RESULTS AND DISCUSSION

Fig. 3.8 and Fig. 3.9 show the measured ^{55}Fe spectrum for different pixel pitches and bias voltages, V_{sub} , respectively. The Mn- K_{α} peak is clearly visible for all versions, indicating near full depletion can be reached for both pixel pitches and at all bias voltages.

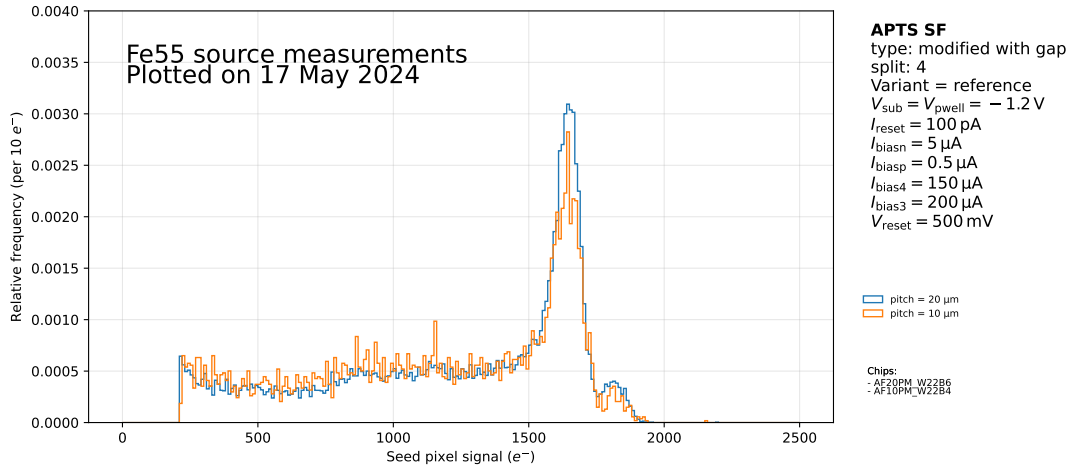


Figure 3.8: **Pitch Comparison:** Distribution of seed signal in e^- for different pixel pitches. The sensors show similar charge collection properties for both pitches.

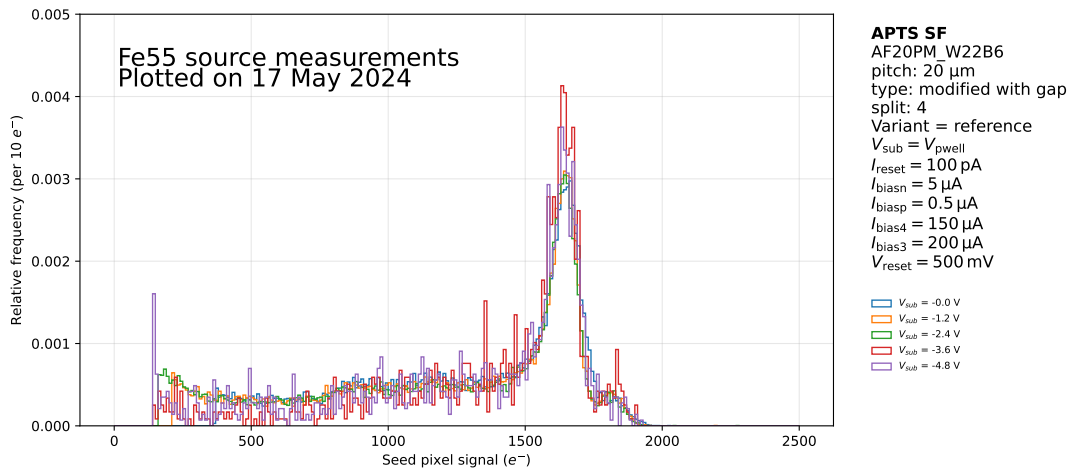


Figure 3.9: **Voltage Comparison:** Distribution of seed signal in e^- for different bias voltages. The sensors show similar charge collection properties for all five bias voltages.

3.2. RESULTS AND DISCUSSION

Comparing sensors with three different irradiation levels in Fig. 3.10 shows a drastic difference between the 10^{15} 1 MeV $n_{\text{eq}} \text{ cm}^{-2}$ irradiated sensor and the other two. Up to an irradiation level of 10^{14} 1 MeV $n_{\text{eq}} \text{ cm}^{-2}$ the charge distribution is comparable with the none-irradiated sensor, illustrating that all generated charge gets collected. However, for the 10^{15} 1 MeV $n_{\text{eq}} \text{ cm}^{-2}$ irradiated sensor, the Mn- K_{α} peak from the ^{55}Fe source is not visible any more, meaning the charge gets trapped and lost due to the radiation damage. This reduction in collected charge was not so strongly observed for the p-type chips with only the reference variant [19], showing that the increased noise in the multiplexer chip causes problems at higher irradiation levels. Since the Mn- K_{α} peak was not visible any more, no fit of it could be performed, which made it impossible to calculate the calibration factor, and it was therefore excluded from the test beam studies presented in Chapter 4.

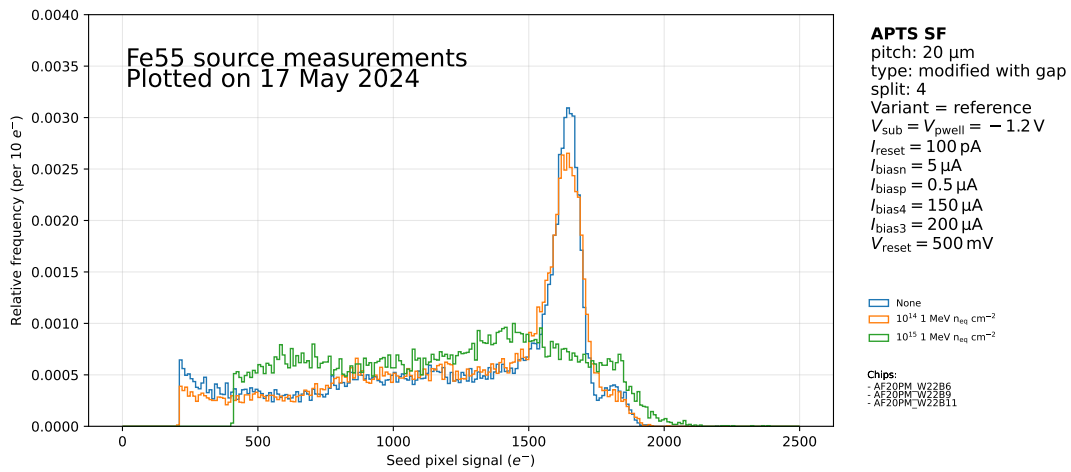


Figure 3.10: **Irradiation Comparison:** Distribution of seed signal in e^- for different irradiation levels. Up to an irradiation of 10^{14} 1 MeV $n_{\text{eq}} \text{ cm}^{-2}$ similar charge collection properties, with irradiation of 10^{15} 1 MeV $n_{\text{eq}} \text{ cm}^{-2}$ the ^{55}Fe peaks are not visible any more.

4 Characterisation with Test Beam

Test beams are an important tool for testing tracking and vertex detectors. They allow testing of the detectors under real but controlled conditions and enable the determination of crucial properties, such as detection efficiency and spatial resolution. In a test beam, a *telescope* is used. It consists of layers of reference sensors, called reference planes and the device under test (DUT), is placed between the reference planes. As particles from the beam pass each plane, they deposit energy in each sensor according to Eq. 2.1.1. The recorded hits from the reference planes are read out and used to reconstruct the trajectory of the particles, the tracks. A window gets defined where the hit position on the DUT is expected. If the centre of mass of a cluster is found on the DUT within that window, the cluster is associated to that particular track. From this, the spatial resolution and detection efficiency of the DUT can be determined.

This chapter first describes the measurement setup. Next follows the description of the analysis of the data taken during the test beam, which is split into two parts. As a first step, the global efficiency and spatial resolution are determined at different thresholds. These results show the overall performance of the sensors and determine the usability of the sensors. In the second part, the efficiency within the pixel is calculated, which gives insight into the charge collection properties of the APTS.

4.1 Methods

Test beams were conducted at the CERN Proton Synchrotron (PS) [34] and Super Proton Synchrotron (SPS) [35] facilities. In total, three test beams were conducted, each lasting one week, with two in March 2023 and one in July 2023. This discussion focusses on the July test beam at

the SPS-Q54 beam line, utilising a 120 GeV hadron beam. During this test beam, the multiplexer chips previously tested in the lab at UZH were evaluated; for reference, see Table 2.2.

4.1.1 Test Beam Setup

The sensors were tested at $V_{\text{sub}} = 0.0 \text{ V}$ and -1.2 V since lab measurements showed that full depletion can already be achieved at these voltages. The telescope used for this test beam consists of six ALPIDE planes which are used as reference planes, providing a tracking resolution of the telescope of $\sigma_{\text{track}} = 2.11 \text{ }\mu\text{m}$ [36].

The DUT and a trigger (TRG) were positioned between the first three and the last three reference planes, as illustrated in Fig. 4.1. The TRG, also an APTS, was mounted on a movable stage such that it could be aligned with the DUT. It ensures that only events that pass through the DUT are recorded. The DUT is cooled using a water chiller set at $T = 14 \text{ }^\circ\text{C}$ similar to the lab setup, to ensure controlled and consistent conditions.

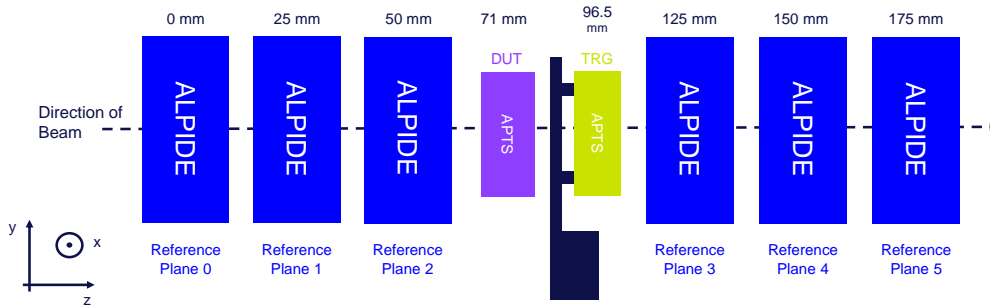


Figure 4.1: Schematic of telescope. Six ALPIDE reference planes (Reference Plane 0-5), in between them the device under test (DUT) and the trigger (TRG) mounted on a movable stage.

The sensors are mounted in a metal box and are connected to the power-supplies and the computer from which everything is controlled, as shown in Fig. 4.2. Additionally, there is a scintillator in the box that is used as a trigger when aligning the telescope to the beam, as well as temperature and humidity sensors to monitor the conditions of the telescope and the DUT. The telescope is placed onto a movable table, which allows to align the telescope to the beam.

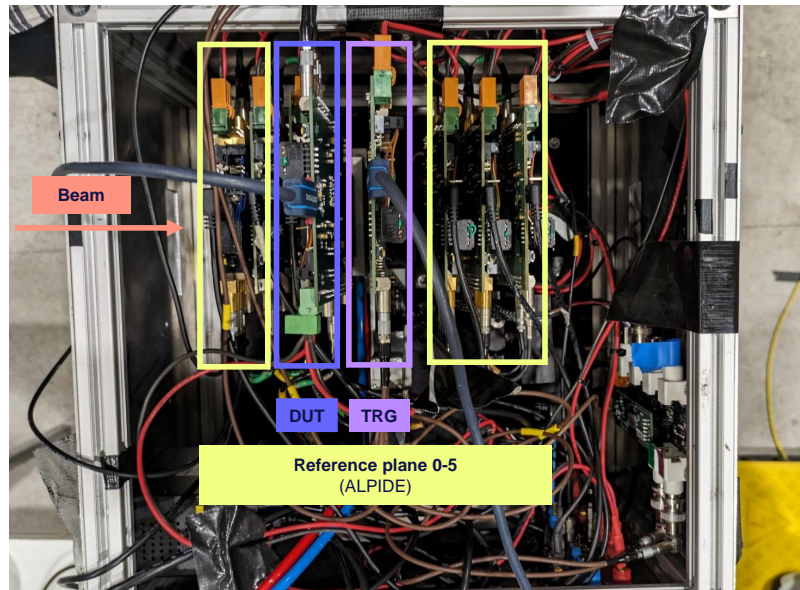


Figure 4.2: Reference planes (ALPIDE), trigger (TRG) and device under test (DUT) mounted inside the metal box.

4.1.2 Analysis with Corryvreckan

Corryvreckan is used to analyse the data collected during the test beam. It is a flexible, versatile, and fast test beam data reconstruction framework following a modular concept. It is used for all 65 nm TPSCo characterisation efforts and is therefore already adjusted for the telescope outlined in Section 4.1.3.

The Corryvreckan reconstruction chain is built via the main configuration file, where separate modules are added for each individual task. The reconstruction chain illustrated in Fig. 4.3 shows the order of modules of the analysis of this test beam data. The geometry of the telescope is defined in a separate geometry file, an excerpt showing the definition of reference plane 0 can be seen in Listing 4.1.

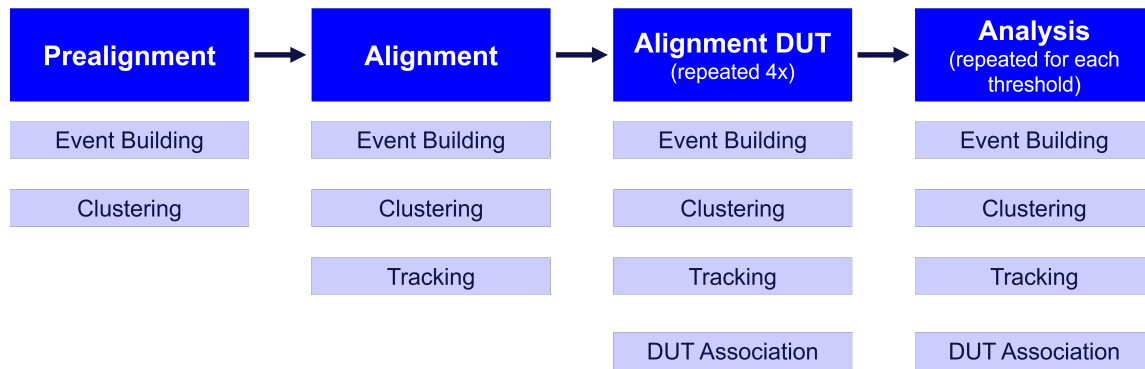


Figure 4.3: Flow chart of analysis chain

```

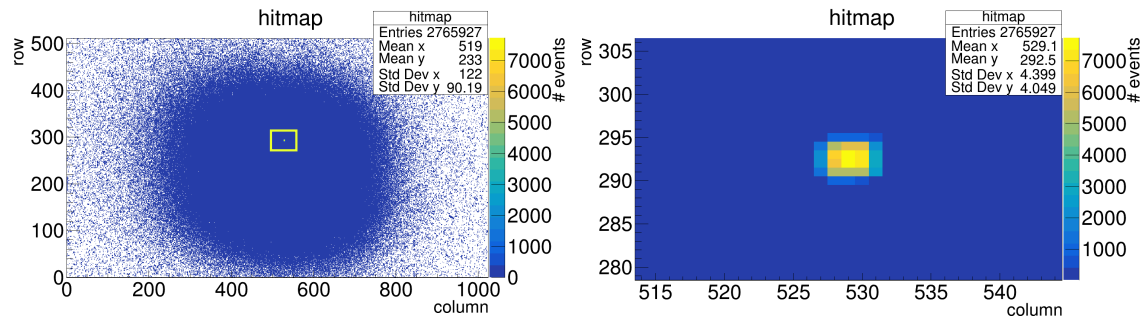
[ALPIDE_0]
coordinates = "cartesian"
mask_file = "/local/output/MaskCreator/ALPIDE_0/mask_ALPIDE_0.txt"
material_budget = 0.001
number_of_pixels = 1024, 512
orientation = 0deg,180deg,0deg
orientation_mode = "xyz"
pixel_pitch = 29.24um,26.88um
position = 0um,0um,0um
roi = [[540,270],[540,307],[574,307],[574,270]]
role = "reference"
spatial_resolution = 5um,5um
time_resolution = 2us
type = "alpide"
.
.
.

```

Listing 4.1: Excerpt of geometry file: definition of reference plane 0

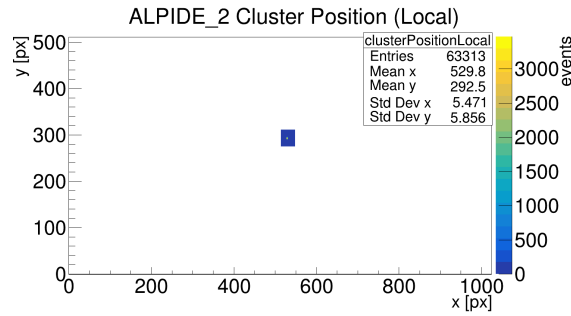
The **event building** module prepares hit information from all detectors, including tasks such as decoding of raw data and the application of charge or hit-time calibrations. Subsequent modules in the reconstruction chain can then only access defined events [37].

An example of a hit-map of a reference plane can be seen in Fig. 4.4a. The blue halo is due to the size of the beam, while the TRG position, where the most hits are collected, is highlighted in the yellow box. Fig. 4.4b provides a zoomed-in view of the same hit-map, focussing on the TRG position. A region-of-interest (ROI) is defined which selects the region around the TRG, as shown in Fig. 4.4c. This allows restricting the selection of tracks or clusters to only relevant regions of the sensors and speeds up the analysis [37].



(a) Beam highlighted in yellow box

(b) Zoomed in on beam



(c) Selected region-of-interest (ROI)

Figure 4.4: Hit-map of reference plane 2

Clustering calculates clusters via a closest neighbour search from all signals of a detector plane, followed by determining the hit position using a charge-weighted centre-of-gravity algorithm [37].

For **tracking** the module TRACKING4D is used. It connects all combinations of hits in the first and last reference plane to form straight lines. Hits in the other reference planes are added if they are within defined spatial and time cuts, updating the reference track at each step. The DUT is excluded from the track finding. The trajectory model used in this analysis is the general-broken-lines model, which accounts for uncertainties from position measurement and scattering between planes [37].

The **DUT Association** establishes an association between clusters on the DUT and a reconstructed track. The distance of a cluster's nearest pixel to the track intercept is evaluated against a spatial cut. If the distance is bigger than the defined spatial cut, the track is not associated with the cluster in the DUT [37].

An **alignment** procedure is necessary as the measurements in the geometry file, containing the position and orientation of each detector plane, cannot be measured precisely enough by hand. The X- and Y-positions as well as the precise orientation strongly influence the track reconstruction. A misalignment of a fraction of a millimetre might already correspond to a shift by multiple pixel pitches. Consequently, an iterative alignment procedure is needed, where the detector planes are shifted and rotated step by step relative to the detector defined as the reference (in this case, reference plane 0) [37].

The alignment procedure aims to centre the track residuals on all planes around zero. Residuals are defined as the distance between the position of the detected hit and the intersection point of the modelled track with the sensor that recorded the hit. The width of the residuals depends on the tracking resolution of the telescope and should be minimised [37].

The alignment of the reference planes and the DUT are done separately and is a two-step procedure, the prealignment and the alignment. The prealignment focusses only on the translational alignment of the planes without changing the rotational alignment. In this analysis, the mean of a Gaussian fit is utilized to determine the translational shifts.

The prealignment of the DUT follows the same strategy as for the reference planes, by modifying the position of the DUT in the geometry file.

For the alignment, the module ALIGNMENTMILLEPEDE is used. It enables a simultaneous fit of the tracks and the alignment constants [37].

The alignment strategy for the DUT again is similar as for the reference planes and requires multiple iterations (here 4 repetitions). But now the algorithm optimises the residuals of the tracks through the DUT.

Once the alignment is done, the residuals should be narrow and centred around zero and a good distribution of the track χ^2/ndf , indicating how well the data fits to the chosen track model. The improvement in χ^2/ndf from the prealignment to the last step of the alignment can be seen in Fig. 4.5a and Fig. 4.5b. Good examples of the residuals of the DUT can be seen in Fig. 4.6a and Fig. 4.6b.

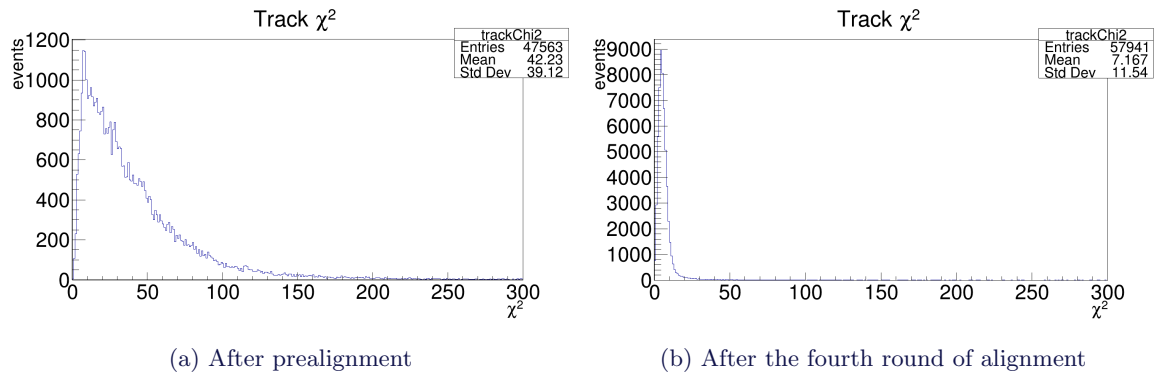
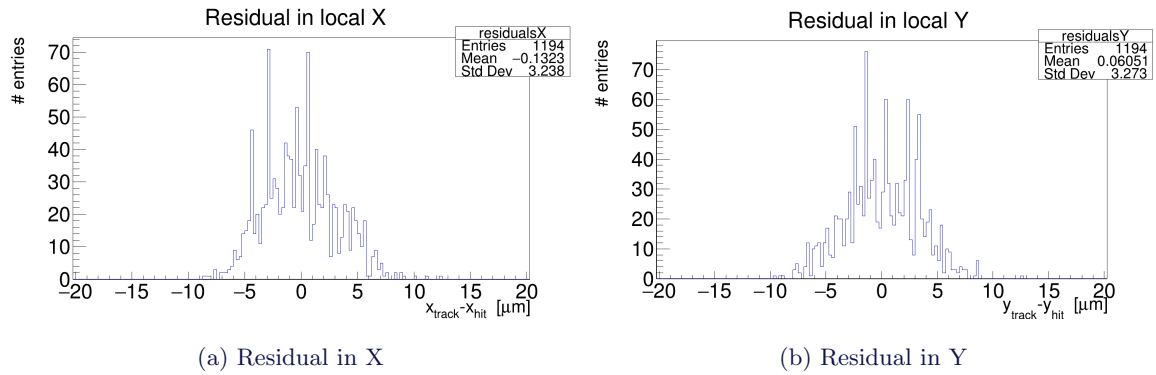
Figure 4.5: Track χ^2/ndf 

Figure 4.6: Residuals of DUT after alignment

The **analysis** of the DUT performance determines different parameters, such as detection efficiency or spatial resolution. The spatial resolution is defined as the root-mean-square of the residuals. The global detection efficiency is calculated as the number of tracks with an associated DUT cluster divided by the total number of tracks passing through the detector. In-pixel studies were performed to identify areas of the pixel where the detection efficiency is decreased. The in-pixel detection efficiency is derived by mapping the efficiency inside a single pixel cell, folding all the track positions inside the pixels of the sensor into a single one [37, 38].

The measurements were taken in runs, with each run containing 50000 triggered events. The analysis reduces the number of events to around 1000-2000 good events where the track could be reconstructed and found on the DUT. For global efficiency and spatial resolution, one run provides sufficient statistics to obtain results with small errors. To determine the in-pixel detection efficiency, however, more than ten times the number of events is needed to reach reasonable results. Therefore, many runs, each taking approx 20 minutes at SPS, needed to be combined.

4.1.3 Temperature Dependence of Alignment

Alignment is the most time-intensive aspect of the analysis. Consequently, it was standard practice to align only the initial run when multiple measurement runs occurred consecutively without alterations to the DUT or disruptions to the setup. This initial alignment was then used for the analysis of all the subsequent runs until there was any movement or disturbance of the DUT or the trigger.

However, during the analysis of this thesis, it was observed that doing this leads to a residual change of the DUT over time by several micrometres. The change of residual could be related to the temperature change. This can be seen in Fig. 4.7. The DUT is cooled using the water chiller, and with this its holder is automatically cooled as well. Therefore, the DUT and its holders are kept at a relatively constant temperature of around 15 °C. The reference planes, the trigger and all their holders however are not cooled and, therefore, follow the changes of the ambient temperature in the box. All the electronics in the box can increase the temperature in it over time by over 10 °C. The reference planes and their holders therefore undergo thermal expansion and move relative to the cooled and stable DUT leading to the change in residual of the DUT.

To confirm this, the analysis was run assuming reference plane 2 as the DUT. Reference plane 2 is also not cooled and should therefore not move relative to the other five reference planes, hence the residual should stay constant. This can be seen in Fig. 4.7.

The solution to this problem is to individually align each run. Doing this will ensure that the residual does not change significantly with time, as can be seen in Fig. 4.7.

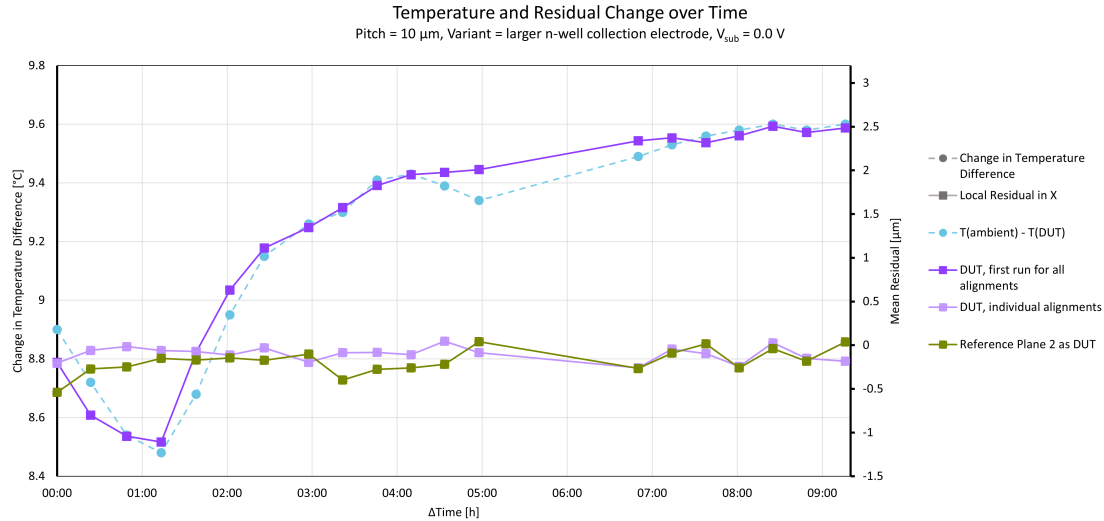


Figure 4.7: Residual change with temperature. Blue: Change of temperature difference between ambient temperature and DUT temperature. Dark purple: Residual of DUT using alignment of first run for all subsequent runs. Light purple: Residual of DUT with each run aligned individually. Green: Residual of reference plane 2 as DUT

4.2 Results and Discussion

In this section, the results derived from the analysis of the test beam data are presented and interpreted. The focus is on the global detection efficiency and spatial resolution of the DUT, as well as the in-pixel detection efficiency. By evaluating these metrics of various sensors across several thresholds, the performance of APTS can be studied.

4.2.1 Global Detection Efficiency and Spatial Resolution

All the results are plotted for thresholds above 3 times the root-mean-square (RMS) of the noise distribution, since running at lower thresholds the signal-to-noise ratio would be very low. The cut on the threshold is performed offline in Corryvreckan and not by setting a threshold in the devices. The thresholds are given in e^- which were converted from ADC units for each sensor with the conversion factor obtained from the radioactive source measurements in Chapter 3.

Fig. 4.8 shows the detection efficiency versus the threshold for the different p-well and n-well collection electrode variants of a $10\ \mu\text{m}$ pitch sensor. For comparison, measurements of a p-type sensor from another test beam were included. All the variants achieve the required detection efficiency of above 99 %, with a good operating range of thresholds where this is achieved. The zoomed-in part of the plot shows that not all variants start at the same threshold but all start at a higher threshold than the p-type. As already seen in the test-pulsing, in Section 3.2.1, the multiplexer chips tend to have more noise because they host four matrices rather than just one. The pixel geometry variant starting at the highest threshold is the *larger n-well collection electrode* due to its higher capacitance, making it more prone to noise. However, overall, all variants exhibit similar performance to the p-type sensor.

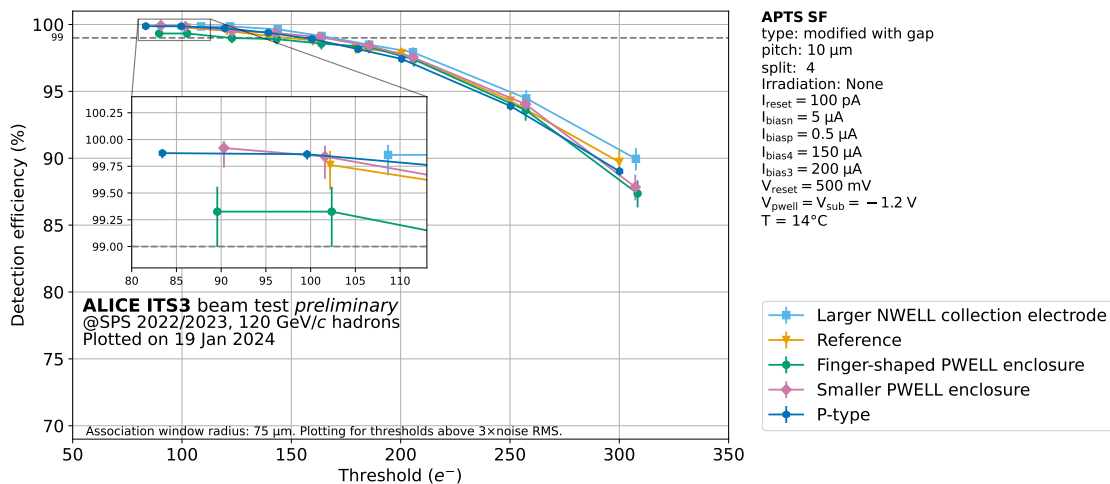


Figure 4.8: **Variant Comparison:** detection efficiency vs threshold. All variants have a good range of operation with over 99 % detection efficiency.

4.2. RESULTS AND DISCUSSION

The spatial resolution versus threshold for the same 10 μm pitch sensor is depicted in Fig. 4.9. All variants reach a very good spatial resolution of less than 3 μm , surpassing the binary resolution of $\text{pitch}/\sqrt{12}$, thanks to charge sharing indicated by an average cluster size of 1.1 - 1.7 pixels.

The only variant standing out is the *larger n-well collection electrode*, with its spatial resolution being slightly worse than of the other variants, due to having less charge sharing and having a higher capacitance making it more prone to noise.

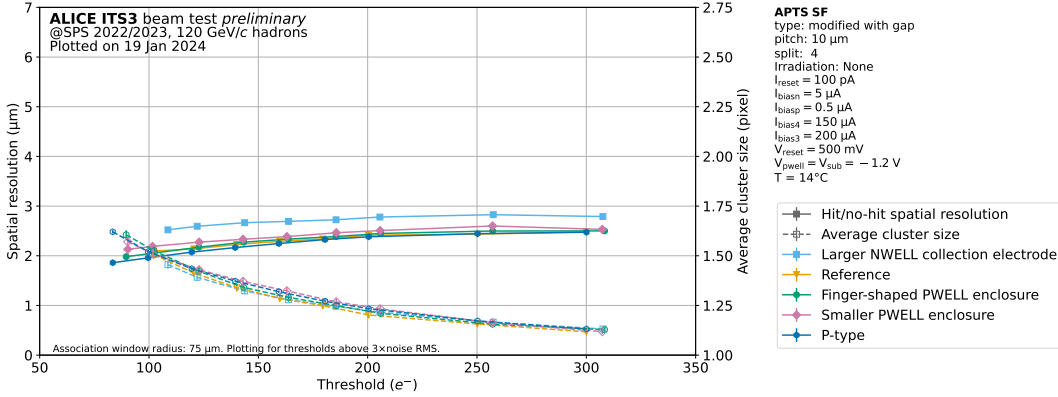


Figure 4.9: **Variant Comparison:** spatial resolution vs threshold. All variants reach better resolution than the binary resolution of $\text{pitch}/\sqrt{12}$, the *larger n-well collection electrode* has slightly worse resolution than the other variants.

The comparison of the 10 μm pitch sensor to the 20 μm pitch sensor focusses specifically on the reference variant. A detailed analysis of all variants of the 20 μm pitch sensor is provided in Appendix A.1, though no significant differences in behavior relative to the 10 μm pitch variants were observed.

The comparison reveals that the 20 μm pitch sensor exhibits slightly better detection efficiency at the same threshold, as shown in Fig. 4.10. It has a larger range of operation, where it reaches a detection efficiency of over 99 %. The 10 μm pitch sensor performs worse due to its increased charge sharing, which reduces its detection efficiency. The difference in spatial resolution is shown in Fig. 4.11. The spatial resolution of the 20 μm pitch sensor is worse, mainly because of its larger pitch size. However, the 20 μm pitch sensor also reaches a resolution better than the binary resolution of $\text{pitch}/\sqrt{12}$ due to charge sharing.

4.2. RESULTS AND DISCUSSION

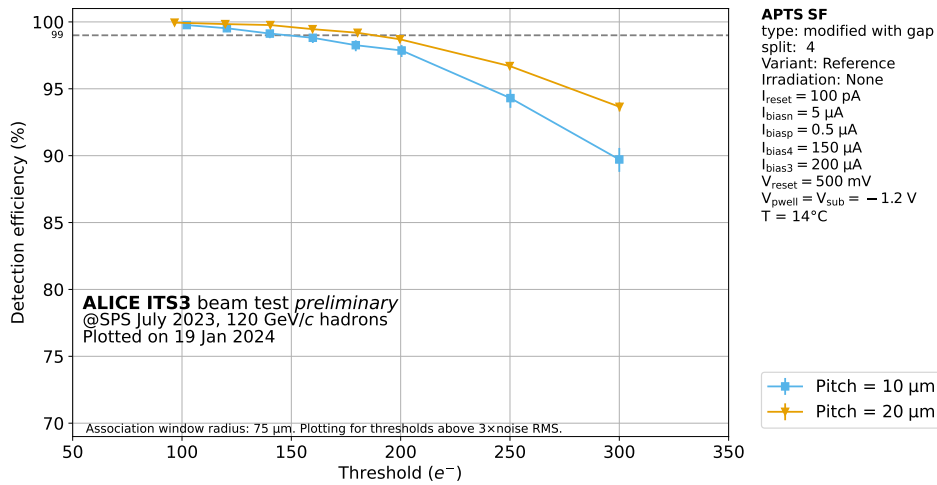


Figure 4.10: **Pitch Comparison:** detection efficiency vs threshold. Both pitches have good range of operation with over 99 % detection efficiency. The 10 μm range is reduced because it has increased charge sharing.

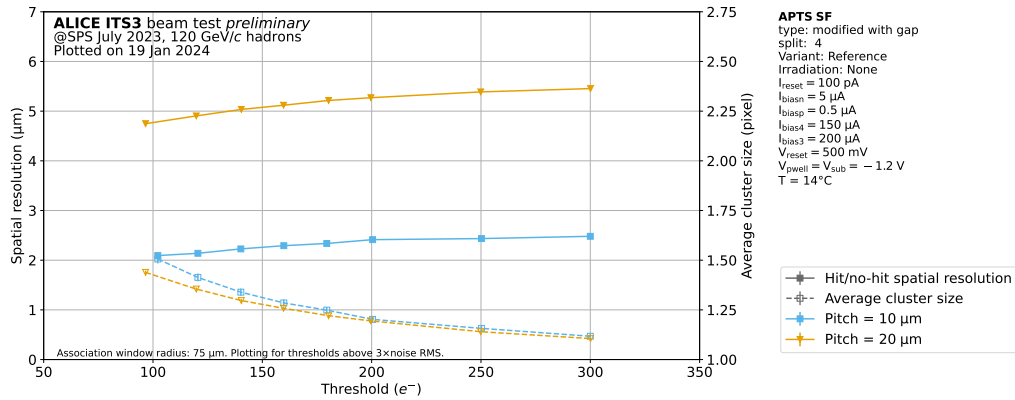


Figure 4.11: **Pitch Comparison:** spatial resolution vs threshold. Both pitches have a better spatial resolution than the binary resolution of $\text{pitch}/\sqrt{12}$.

Fig. 4.12 shows the efficiency of a 20 μm pitch sensor irradiated with $10^{14} \text{ 1 MeV } n_{\text{eq}} \text{ cm}^{-2}$. It still reaches a detection efficiency above 99 % and maintains a good range of operation, making it still

usable. The different variants exhibit the same behaviour as discussed previously for the 10 μm non-irradiated case shown in Fig. 4.8.

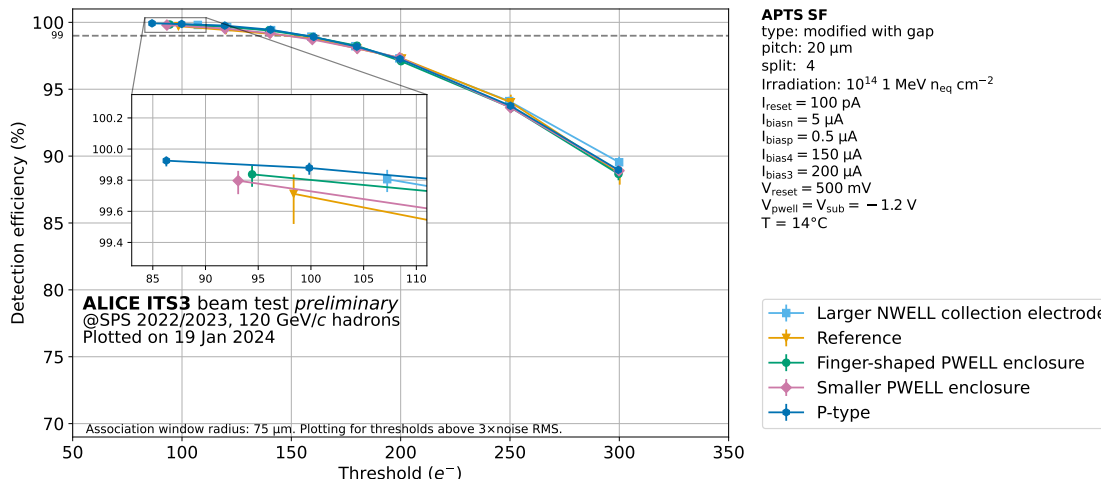


Figure 4.12: **Radiation Hardness:** detection efficiency vs threshold. After irradiation of 10^{14} 1 MeV $n_{\text{eq}} \text{cm}^{-2}$, all variants still have a good range of operation with over 99 % detection efficiency

In contrast to this, the behaviour of the variants differs for the spatial resolution from the non-irradiated case. Fig. 4.13 shows that now all variants have the same spatial resolution and the *larger n-well collection electrode* no longer stands out like in Fig. 4.9. The performance of the *larger n-well collection electrode* is less degraded by radiation than that of the other variants. While the spatial resolution of the other variants worsens with irradiation, the spatial resolution of the *larger n-well collection electrode* stays nearly the same. Consequently, the spatial resolution of the other variants converges towards that of the *larger n-well collection electrode*. Nevertheless, the performance of the *larger n-well collection electrode* variant remains either worse than the other variants (non-irradiated case) or is equivalent to theirs (irradiated case).

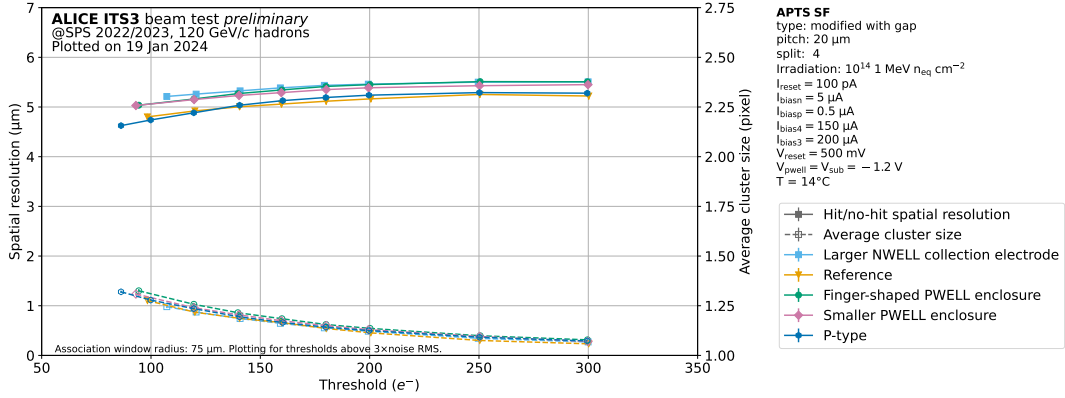


Figure 4.13: **Radiation Hardness:** spatial resolution vs threshold. After irradiation of 10^{14} 1 MeV n_{eq} cm^{-2} , all variants reach similar spatial resolution, the better performing variants having converged to the worse *larger n-well collection electrode* resolution of the non-irradiated case.

As mentioned in Section 3.2.2 and shown in the ^{55}Fe spectrum plot in Fig. 3.10, the results of the 10^{15} 1 MeV n_{eq} cm^{-2} were not analysed, since it was impossible to determine the cluster conversion factor from the measurements with the radioactive source. Results from p-type sensor measurements showed that for 10 μm pitch sensors irradiated up to 10^{15} 1 MeV n_{eq} cm^{-2} , a detection efficiency of almost 99 % can still be reached even at a voltage of 0 V. This can be explained by the decreased collection volume, which leads to a reduced leakage current, thus minimising noise, and a lower charge loss for smaller pitches after irradiation. [19].

Because near-full depletion was already achieved at $V_{sub} = 0.0$ V and - 1.2 V, as seen in Fig. 3.9, the voltage comparison plots are not shown here. An example showing the difference between $V_{sub} = 0$ V and - 1.2 V can be found in the appendix A.1.

In general, there are no significant differences between the variants. All of them provide a good range of operation, where they reach the needed detection efficiency of over 99 %. The 10 μm pitch sensors reach an exceptional spatial resolution of less than 3 μm, fulfilling the FCC-ee spatial resolution requirements. The radiation hardness requirements are also met by working up to 10^{14} 1 MeV n_{eq} cm^{-2} .

4.2.2 In-Pixel Detection Efficiency

The goal of the in-pixel study was to pinpoint areas within the pixel where the detection efficiency loss occurs. To achieve this, many measurement runs were combined and the results of all measured pixels are overlaid to reach a sufficient statistical significance.

Fig. 4.14 and Fig. 4.15 present results from a non irradiated 10 μm reference variant sensor at $V_{\text{sub}} = -1.2$ V. Fig. 4.14 shows the results for a threshold of 140 e^- where the global detection efficiency exceeds 99 %, indicating optimal operational conditions. Fig. 4.15 corresponds instead to a threshold of 250 e^- where the global detection efficiency is significantly decreased, highlighting the specific areas within the pixel where the detection efficiency is reduced.

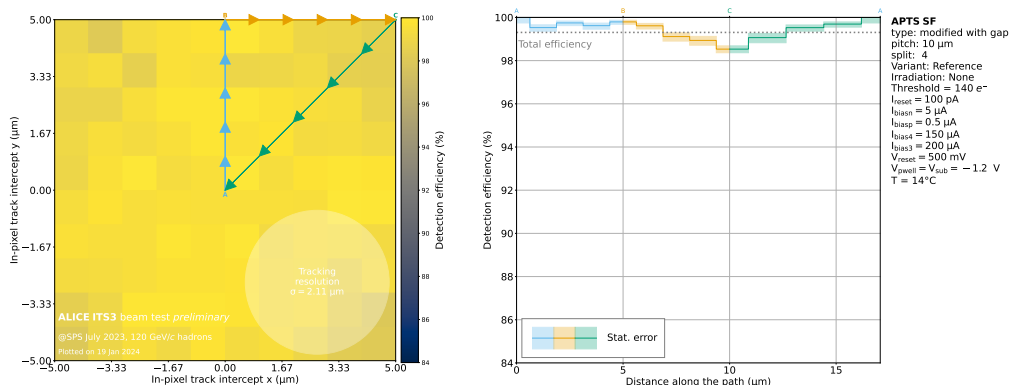


Figure 4.14: In-pixel detection efficiency at threshold of 140 e^- . Left: A single pixel divided into bins, each representing the local detection efficiency. Right: Efficiency variation along different paths within the pixel. Blue path indicates efficiency from the middle of the pixel (A) to the edge (B), orange path shows efficiency along the edge to the corner (C), and green path illustrates efficiency from the corner back to the middle (A).

On the left side of the plots, a single pixel is depicted, divided into bins. Each bin represents the detection efficiency at that position. The plots on the right-hand side illustrate the variation in detection efficiency along different paths. The blue path represents the detection efficiency from the middle of the pixel (A) to the edge (B). The orange path represents the detection efficiency along the edge, from B to the corner (C). The green path illustrates the detection efficiency from

4.2. RESULTS AND DISCUSSION

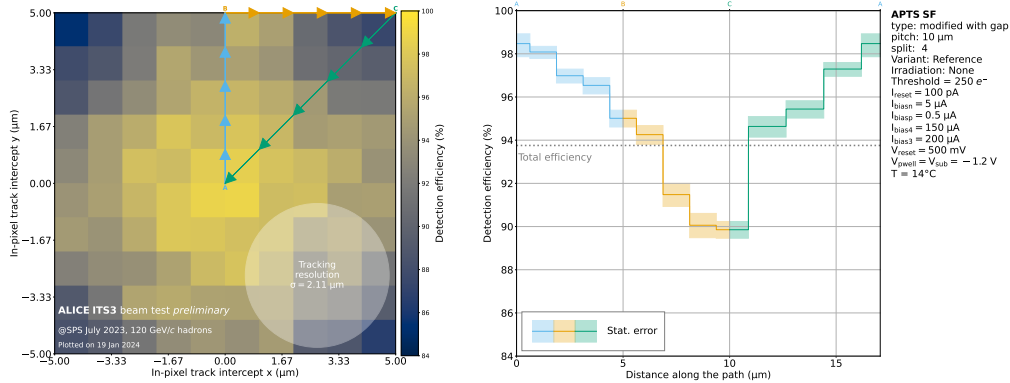


Figure 4.15: In-pixel detection efficiency at threshold of $250 e^-$. Left: A single pixel divided into bins, each representing the local detection efficiency. Right: Efficiency variation along different paths within the pixel. Blue path indicates efficiency from the middle of the pixel (A) to the edge (B), orange path shows efficiency along the edge to the corner (C), and green path illustrates efficiency from the corner back to the middle (A).

the corner back to the middle (A). The gray line indicates the global efficiency for the reported threshold, corresponding to the global detection efficiency reported in Fig. 4.8.

For a threshold of $140 e^-$, the global detection efficiency still reaches 99 % and the efficiency is nearly uniform over the whole pixel. Although a slight drop in detection efficiency can already be observed in the corners, where it does not reach 99 % efficiency any more.

At higher thresholds, areas where detection efficiency is lost become more visible. In Fig. 4.15 at threshold $250 e^-$, the global detection efficiency is just below 94 %, in the corners it drops to around 90 % while in the middle it is still around 99 %. It becomes apparent that the in-pixel detection efficiency is worst at the corners and edges of the pixel. This is because here charge sharing with the neighbouring pixel occurs, resulting in incomplete charge collection by one pixel. This effect is most pronounced at the corners of the pixel, where charge sharing happens with three other pixels. In the centre of the pixel, however, the detection efficiency stays high, since this is where the collection electrode is.

Fig. 4.14 and Fig. 4.15 show the behaviour of a reference variant of a 10 μm pitch sensor. It is noteworthy that the other variants behaved very similarly, and the comparison to the 20 μm pitch

sensors also show the same behaviour. Plots of the other variants and of the 20 μm pitch sensor can be found in the appendix [A.2](#). Furthermore, similar drops in detection efficiency at the edges and corners were observed for the *Digital Pixel Test Structure* (DPTS) at higher irradiation levels [\[33\]](#).

5 Conclusion and Outlook

To study the centrepiece of the SM, the Higgs boson, in detail, a new particle collider is needed. One of the proposed future collider projects is the FCC. It is a very versatile collider that goes beyond the sole study of the Higgs boson but offers the opportunity to study the SM in its entirety, including the study of the electroweak sector and many QCD processes, the top quark, and flavour physics to a precision beyond LHCb and Belle-II. For all of these physics goals, excellent vertex reconstruction is needed, especially for the measurements of the Higgs-to-quark couplings and the flavour physics.

This thesis aimed to assess the feasibility of meeting the FCC-ee vertex detector's requirements and even to achieve a better performance than that. ALICE ITS3 is featuring similar vertex detector requirements as the FCC-ee. This thesis studies the APTS MAPS prototype, developed in this context, focussing on the performance of the pixel geometry variants.

The characterisation of APTS was carried out with a radioactive source in the lab at UZH and at test beams at PS and SPS at CERN. This allowed the extensive study on charge collection properties, spatial resolution and global and in-pixel detection efficiency.

The results indicate that all variants, regardless of pitch or bias voltage, collected nearly all of the generated charge. This suggests that the epitaxial layer is close to full depletion. Although the *larger n-well collection electrode* pixel geometry, having a higher capacitance, is more prone to noise. This trend can be observed in the detection efficiency as well. While all variants reached 99 % efficiency with a good range of operation, the *larger n-well collection electrode* starts at a slightly higher threshold because it is more affected by noise.

The in-pixel study revealed that the detection efficiency loss occurs in the edges and corners of the pixel, which is expected since there more charge sharing and longer drift times occur which reduces the efficiency.

The spatial resolution shows the effect of pixel pitch and charge sharing. Both tested pitches, 10 μm and 20 μm , reach a resolution better than the binary resolution of $\text{pitch}/\sqrt{12}$. The 10 μm pitch reaches an exceptional resolution of less than 3 μm , already meeting the spatial resolution requirements of the FCC-ee vertex detectors.

The comparison of sensors with different irradiation levels demonstrated that the APTS reach 99 % detection efficiency with a good range of operational thresholds up to irradiation levels of 10^{14} 1 MeV $n_{\text{eq}} \text{ cm}^{-2}$, meeting the radiation hardness requirements of the FCC-ee vertex detectors. Here, a slight difference in the performance of the different variants could be observed. While the *smaller p-well, reference* and *finger-shaped p-well* variants perform slightly worse after irradiation, the *larger n-well collection electrode* is less effected by radiation damage, maintaining its spatial resolution after irradiation of 10^{14} 1 MeV $n_{\text{eq}} \text{ cm}^{-2}$. Before irradiation, the *larger n-well collection electrode* initially has a worse spatial resolution than the other three variants, while after irradiation the performance of the other three variants converges to the same spatial resolution.

Compared to a normal p-type sensor, multiplexer sensors tended to perform slightly worse, probably due to increased noise from powering four matrices simultaneously. However, the difference between multiplexer and p-type sensors was minimal and no pixel geometry variant stood out significantly, concluding the investigation of different pixel geometries.

In general, no significant performance differences were observed between variants independent of pitch, irradiation level or bias voltage. Each variant exhibited robust performance, meeting spatial resolution and irradiation hardness requirements for FCC-ee vertex detectors. Considering that APTS was not designed with the FCC-ee requirements in mind and that there is still more than ten years for technology to advance before the construction of the FCC-ee detector could start, the results are promising for the feasibility of the FCC-ee vertex detector. Moreover, as ALICE ITS3 goes beyond the requirements of the FCC-ee in terms of material budget and power consumption, there is potential for achieving a performance surpassing the original FCC-ee expectations, e.g. by adapting a curved wafer-scale MAPS layout also to FCC-ee [15, 28].

The extensive study of APTS concluded at the end of 2023. The study investigated different process designs, pixel pitch sizes, irradiation levels, p-well and n-well collection electrode variants and more.

This thesis contributed significantly to the study of the four pixel geometry variants. The overall results show that the sensor performance required by the ITS3 detector design is feasible. The paper *Characterisation of analogue Monolithic Active Pixel Sensor test structures implemented in a 65 nm CMOS imaging process* [19] submitted to the journal *Nuclear Inst. and Methods in Physics Research*, presents all the results on the APTS. The findings of this thesis and the APTS research campaign were further presented by the author at the 19th TREDI workshop on advanced silicon radiation detectors [39].

ITS3 moved on to study large stitched prototype sensors and the assembly of wafer-scaled sensors. The Technical Design Report of ALICE ITS3 can be found at [16].

The midterm report of the FCC feasibility study was published in February 2024. It showed great progress towards the overall feasibility of the FCC project. The CERN council is updating the European Strategy for Particle Physics. Inputs can be submitted until March 2025, and the strategy will be updated in June 2026. Ultimately, it is up to the CERN council to decide whether the FCC should be built, with a decision expected for late 2027/early 2028. With the current timeline, the FCC-ee could start taking data and advancing our knowledge of the elementary particles and their interactions starting 2045.

A Appendix

A.1 Spatial Resolution and Global Efficiency

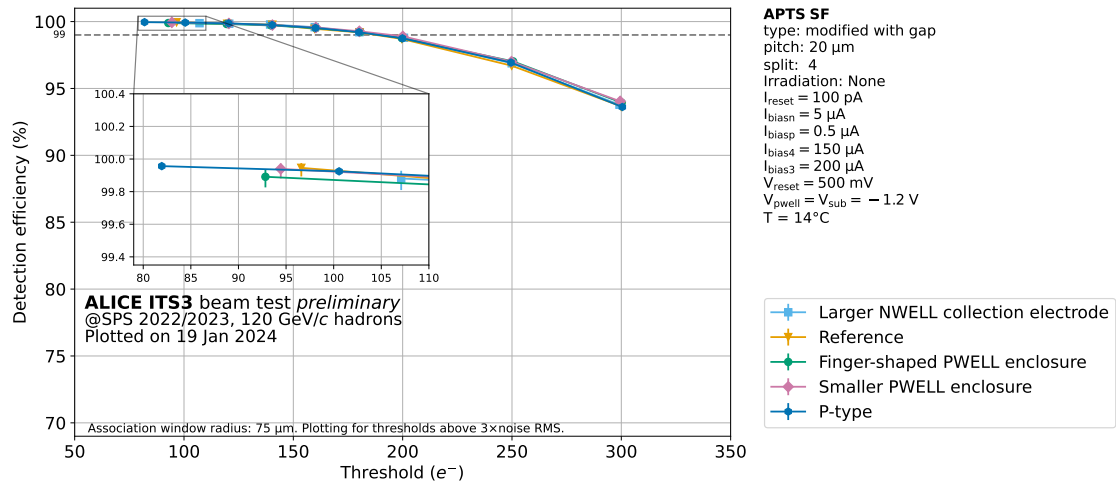


Figure A.1: Detection efficiency: 20 μm variant comparison

A.1. SPATIAL RESOLUTION AND GLOBAL EFFICIENCY

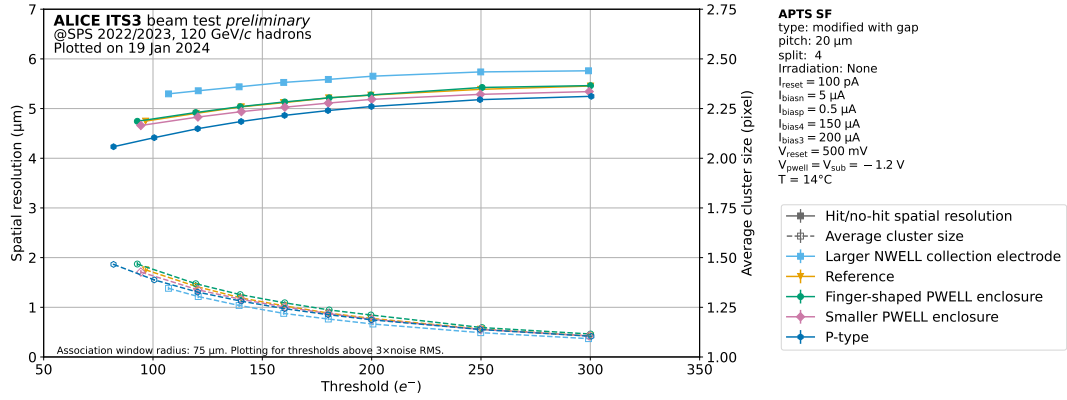


Figure A.2: Spatial resolution: 20 μm variant comparison

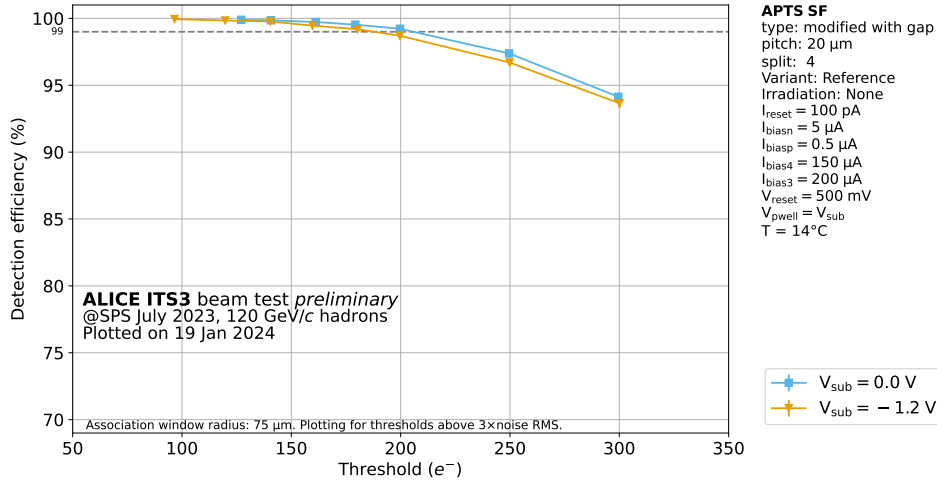


Figure A.3: Detection efficiency: voltage comparison

A.1. SPATIAL RESOLUTION AND GLOBAL EFFICIENCY

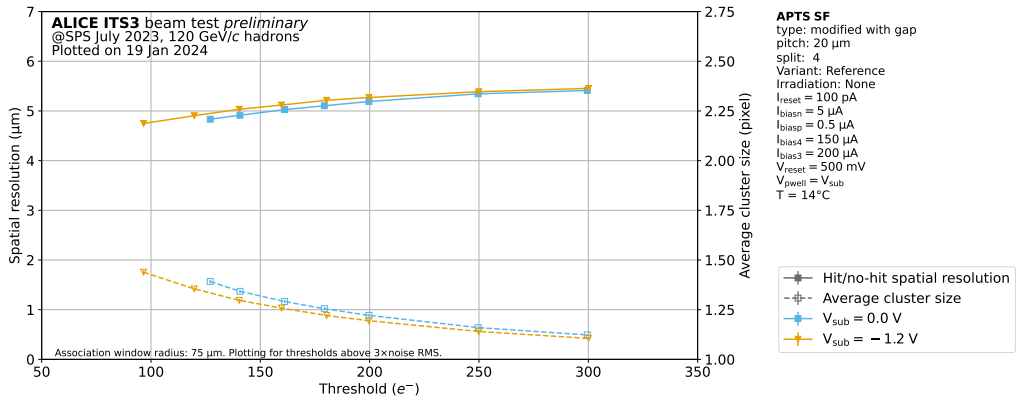


Figure A.4: Spatial resolution: voltage comparison

A.2 In-Pixel Detection Efficiency

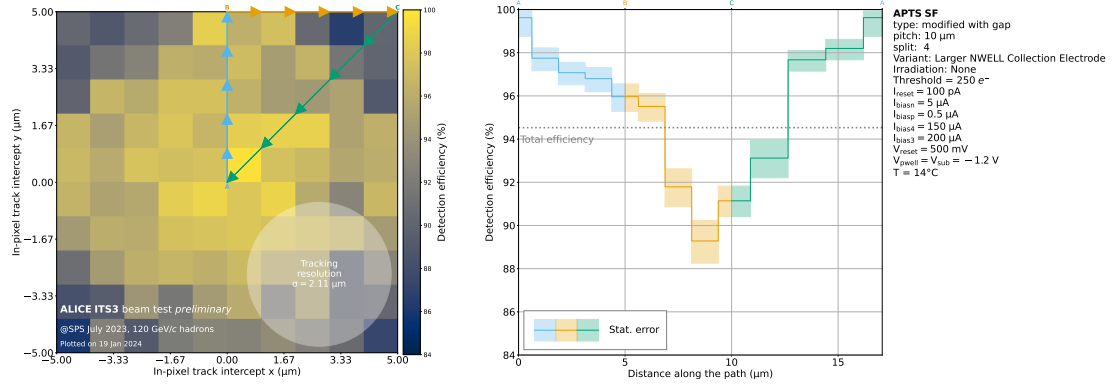


Figure A.5: In-pixel detection efficiency: larger n-well collection electrode variant, 10 μm

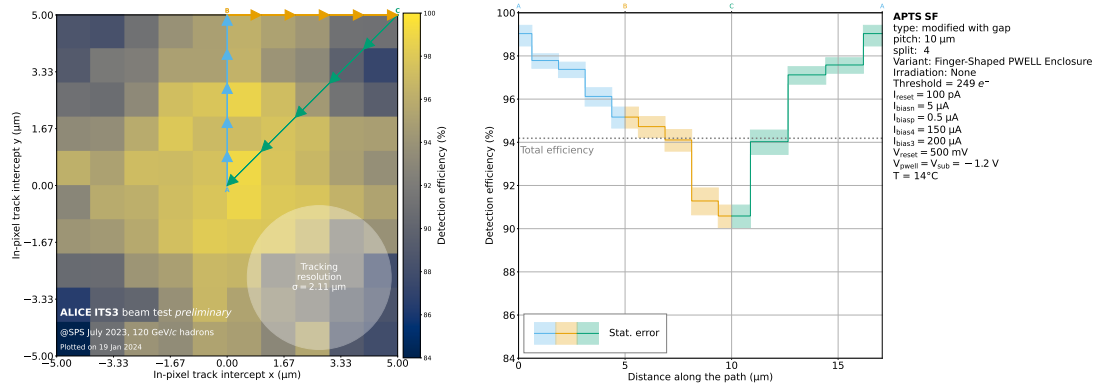


Figure A.6: In-pixel detection efficiency: finger-shaped p-well enclosure variant, 10 μm

A.2. IN-PIXEL DETECTION EFFICIENCY

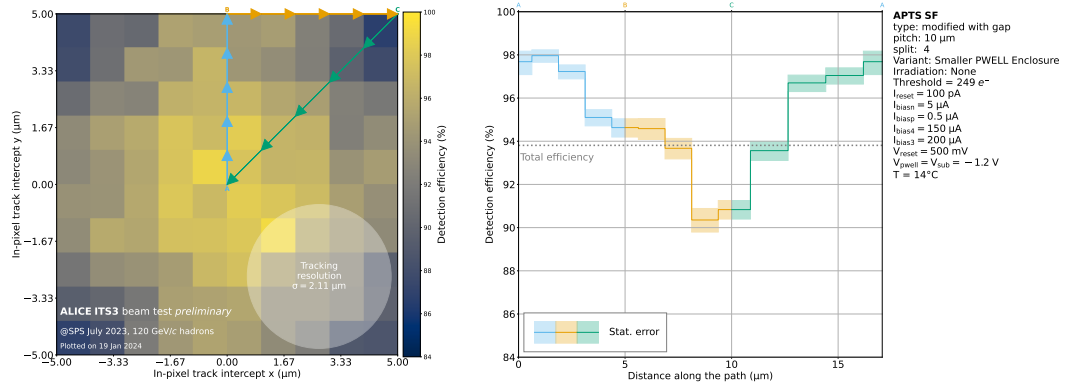


Figure A.7: In-pixel detection efficiency: smaller p-well enclosure variant, 10 μm

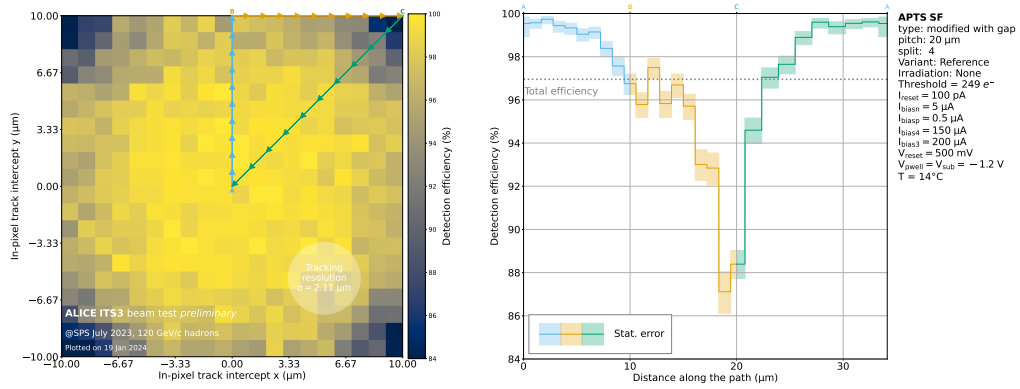


Figure A.8: In-pixel detection efficiency: reference variant, 20 μm

Bibliography

1. Auchmann, B. *et al.* *FCC Midterm Report* Feb. 2024. <https://doi.org/10.17181/zh1gz-52t41>.
2. Bambade, P. *et al.* *The International Linear Collider: A Global Project* 2019. <http://arxiv.org/abs/1903.01629>.
3. The Compact Linear Collider (CLIC) - 2018 Summary Report. *CERN Yellow Reports: Monographs* **Vol. 2**. <https://doi.org/10.23731/CYRM-2018-002> (2018).
4. Accettura, C. *et al.* *Interim report for the International Muon Collider Collaboration (IMCC)* July 2024. <http://dx.doi.org/10.48550/arXiv.2407.12450>.
5. Abdallah, W. *et al.* *CEPC Technical Design Report – Accelerator (v2)* 2023. <http://cds.cern.ch/record/2884908>.
6. Palmer, R. B. & Gallardo, J. C. *High Energy Colliders* 1997. <https://doi.org/10.48550/arXiv.physics/9702016>.
7. Charitos, P. *Future Circular Collider - Image selection* 2019. <https://cds.cern.ch/record/2653532> (2024).
8. Butler, J. N. *et al.* *Report of the 2021 U.S. Community Study on the Future of Particle Physics (Snowmass 2021)* tech. rep. FERMILAB-CONF-23-008-AD-ND-PPD-SCD; SLAC-PUB-17717 (Fermi National Accelerator Lab. (FNAL), Batavia, IL (United States); SLAC National Accelerator Lab., Menlo Park, CA (United States); Lawrence Berkeley National Lab. (LBNL), Berkeley, CA (United States); Argonne National Lab. (ANL), Argonne, IL (United States); Pacific Northwest National Lab. (PNNL), Richland, WA (United States), 2023). <http://dx.doi.org/10.2172/1922503> (2024).

9. Abada, A. *et al.* FCC-ee: The Lepton Collider: Future Circular Collider Conceptual Design Report Volume 2. *The European Physical Journal Special Topics* **228**, 261–623. ISSN: 19516355. <http://dx.doi.org/10.1140/epjst/e2019-900045-4> (2019).
10. Lippmann, C. Particle identification. *Nuclear Instruments and Methods in Physics Research Section A: Accelerators, Spectrometers, Detectors and Associated Equipment* **666**, 148–172. ISSN: 01689002. <http://dx.doi.org/10.1016/j.nima.2011.03.009> (2012).
11. Antonello, M. IDEA: A detector concept for future leptonic colliders. *Il Nuovo Cimento C* **43**, 27. <http://dx.doi.org/10.1393/ncc/i2020-20027-2> (2020).
12. Bacchetta, N. *et al.* CLD – A Detector Concept for the FCC-ee 2019. <https://doi.org/10.48550/arXiv.1911.12230>.
13. Morange, N. Noble Liquid Calorimetry for FCC-ee. *Instruments* **6**, 55. ISSN: 2410390X. <http://dx.doi.org/10.3390/instruments6040055> (2022).
14. Caputo, C. *et al.* Particle identification with the cluster counting technique for the IDEA drift chamber. *Nuclear Instruments and Methods in Physics Research Section A: Accelerators, Spectrometers, Detectors and Associated Equipment* **1048**, 167969. ISSN: 0168-9002. <http://dx.doi.org/10.1016/j.nima.2022.167969> (2023).
15. Ilg, A. *Design and Performance of the IDEA Vertex Detector at FCC-ee in Full Simulation* in *Proceedings of The European Physical Society Conference on High Energy Physics — PoS(EPS-HEP2023)* (Sissa Medialab, Hamburg, Germany, 2023). <http://dx.doi.org/10.22323/1.449.0600>.
16. The ALICE collaboration. *Technical Design report for the ALICE Inner Tracking System 3 - ITS3 ; A bent wafer-scale monolithic pixel detector* tech. rep. CERN-LHCC-2024-003, ALICE-TDR-021 (CERN, Geneva, 2024). <https://cds.cern.ch/record/2890181>.
17. Groom, D. E. & Klein, S. R. Passage of particles through matter. *The European Physical Journal C - Particles and Fields* **15**, 163–173. ISSN: 1434-6052. <http://dx.doi.org/10.1007/BF02683419> (2000).
18. Wilson, T. *Electronic Devices: Lecture 3* 2011.

19. Rinella, G. A. *et al.* *Characterisation of analogue Monolithic Active Pixel Sensor test structures implemented in a 65 nm CMOS imaging process* 2024. <https://doi.org/10.48550/arXiv.2403.08952>.
20. Calvo, J. *et al.* TRACS: A multi-thread transient current simulator for micro strips and pad detectors. *Nuclear Instruments and Methods in Physics Research Section A: Accelerators, Spectrometers, Detectors and Associated Equipment* **917**, 77–85. ISSN: 0168-9002. <http://dx.doi.org/10.1016/j.nima.2018.11.132> (Feb. 2019).
21. Magliocca, C., Kuhl, T., Vishwakarma, A. & Robin, M. The Transverse Impact Parameter as a Relevant Variable to Study the Adjusted-MC Method in the ATLAS Experiment. *DESY Summer Student Programme* (2018).
22. Wermes, N. *Pixel vertex detectors* 34th SLAC Summer Institute on Particle Physics: The Next Frontier: Exploring with the LHC, 2006.
23. Apadula, N. *et al.* *Monolithic Active Pixel Sensors on CMOS technologies* 2022. <https://doi.org/10.48550/arXiv.2203.07626>.
24. Aglieri Rinella, G. *et al.* Charge collection properties of TowerJazz 180 nm CMOS Pixel Sensors in dependence of pixel geometries and bias parameters, studied using a dedicated test-vehicle: The Investigator chip. *Nuclear Instruments and Methods in Physics Research Section A: Accelerators, Spectrometers, Detectors and Associated Equipment* **988**, 164859. ISSN: 01689002. <http://dx.doi.org/10.1016/j.nima.2020.164859> (2021).
25. Bacchetta, N., Collins, P. & Riedler, P. Tracking and vertex detectors at FCC-ee. *The European Physical Journal Plus* **137**, 231. ISSN: 2190-5444. <http://dx.doi.org/10.1140/epjp/s13360-021-02323-w> (2022).
26. The ALICE collaboration. *Expression of Interest for an ALICE ITS Upgrade in LS3* 2018. <https://cds.cern.ch/record/2644611> (2024).
27. Rinella, G. A. Developments of stitched monolithic pixel sensors towards the ALICE ITS3. *Nuclear Instruments and Methods in Physics Research Section A: Accelerators, Spectrometers, Detectors and Associated Equipment* **1049**, 168018. <http://dx.doi.org/10.1016/j.nima.2023.168018> (2023).

28. Freitag, L. *Benefits of Minimizing the Vertex Detector Material Budget at the FCC-ee* 2023. <https://cds.cern.ch/record/2851362>.
29. Buckland, M. First measurements with monolithic active pixel test structures produced in a 65 nm CMOS process. *Journal of Instrumentation* **19**, C02017. ISSN: 17480221. <http://dx.doi.org/10.1088/1748-0221/19/02/C02017> (2024).
30. Snoeys, W. *et al.* A process modification for CMOS monolithic active pixel sensors for enhanced depletion, timing performance and radiation tolerance. *Nuclear Instruments and Methods in Physics Research Section A: Accelerators, Spectrometers, Detectors and Associated Equipment* **871**, 90–96. ISSN: 0168-9002. <http://dx.doi.org/10.1016/j.nima.2017.07.046> (2017).
31. Munker, M. *et al.* Simulations of CMOS pixel sensors with a small collection electrode, improved for a faster charge collection and increased radiation tolerance. *Journal of Instrumentation* **14**, C05013. ISSN: 17480221. <http://dx.doi.org/10.1088/1748-0221/14/05/C05013> (2019).
32. Bugiel, S. *et al.* Charge sensing properties of monolithic CMOS pixel sensors fabricated in a 65 nm technology. *Nuclear Instruments and Methods in Physics Research Section A: Accelerators, Spectrometers, Detectors and Associated Equipment* **1040**, 167213. ISSN: 0168-9002. <http://dx.doi.org/10.1016/j.nima.2022.167213> (2022).
33. Rinella, G. A. *et al.* Digital Pixel Test Structures implemented in a 65 nm CMOS process. *Nuclear Instruments and Methods in Physics Research Section A: Accelerators, Spectrometers, Detectors and Associated Equipment* **1056**, 168589. ISSN: 01689002. <http://dx.doi.org/10.1016/j.nima.2023.168589> (2023).
34. Steerenberg, R. *et al.* *Fifty years of the CERN Proton Synchrotron : Volume 1* 2011. <https://cds.cern.ch/record/1359959>.
35. Doble, N., Gatignon, L., Hübner, K. & Wilson, E. in *Advanced Series on Directions in High Energy Physics* 135–177 (WORLD SCIENTIFIC, 2017). ISBN: 978-981-4749-13-8 978-981-4749-14-5. http://dx.doi.org/10.1142/9789814749145_0005.
36. Mager, M. *The Telescope Optimiser V1.0* 2016. <https://mmager.web.cern.ch/telescope/tracking.html>.

37. Kröger, J., Spannagel, S. & Williams, M. *User Manual for the Corryvreckan Test Beam Data Reconstruction Framework, Version 1.0* 2019. <https://doi.org/10.48550/arXiv.1912.00856>.
38. Dannheim, D. *et al.* Corryvreckan: a modular 4D track reconstruction and analysis software for test beam data. *Journal of Instrumentation* **16**, P03008. ISSN: 1748-0221. <http://dx.doi.org/10.1088/1748-0221/16/03/P03008> (2021).
39. Wittwer, R. *Characterisation of the Analogue Pixel Test Structures produced in the 65 nm TP-SCo process* 19th TREDI Workshop on Advanced Silicon Radiation Detectors, 2024. <https://agenda.infn.it/event/39042/contributions/221978/>.